A Complete Study of Space-Time-Frequency Statistical Properties of the 6G Pervasive Channel Model

Cheng-Xiang Wang, *Fellow, IEEE*, Zhen Lv, *Member, IEEE*, Yunfei Chen, *Senior Member, IEEE*, and Harald Haas, *Fellow, IEEE*

***Abstract*—The sixth generation (6G) pervasive channel model (6GPCM) can characterize channels for all spectra from the sub-6 GHz band to the visible light communication (VLC) band and all scenarios, such as maritime, (ultra-)massive multiple-input multiple-output (MIMO), and industrial Internet of things (IIoT) communication scenarios in 6G wireless systems. The unified channel model can enable us to analyze channel statistical properties in systems using different scales of antenna arrays, different frequency bands, and different scenarios with different movement speeds. In this paper, we conduct a complete study on space-time-frequency (STF) statistical properties of the 6GPCM. Mathematical derivations and simulations are provided, including STF correlation function (STFCF), spatial/temporal/frequency correlation functions, angular/Doppler/delay power spectral densities (PSDs), root mean square (RMS) angular/Doppler/delay spreads, coherence distance/time/bandwidth, stationary distance/time/bandwidth, and level-crossing rates (LCRs)/average fade durations (AFDs) in STF domains. In addition, we classify these statistical properties according to their definitions and then reveal the complex relationships between them and channel model parameters. This work will lay a solid foundation and offer useful guidelines for research on 6G wireless communication systems.**

***Index Terms*—6G pervasive channel model, channel model parameters, geometry-based stochastic model (GBSM), space-time-frequency non-stationarity, space-time-frequency statistical properties.**

I. INTRODUCTION

THE sixth generation (6G) wireless communication systems are expected to utilize new frequency bands, such as the terahertz (THz) [1] and visible light communication (VLC) [2] bands, and new technologies, such as ultra-massive multiple-input multiple-output (MIMO) [3] and reconfigurable intelligent surface (RIS) [4] to serve space-air-ground-sea integrated communication networks [5]. An insightful understanding of the underlying properties of 6G channels between transmitters (Txs) and receivers (Rxs) is a prerequisite for the system design, theoretical analysis, performance evaluation, optimization, and deployment of 6G wireless communication systems [6], [7].

However, there lacks a comprehensive and in-depth analysis of all 6G channel statistical properties. Most of the studies only focus on a portion of these channel properties. For example, authors in [8] introduced and explained correlation functions (CFs) and the corresponding power spectrum densities (PSDs) of a general space-time-frequency (STF) non-stationary channel. Other channel properties, such as the delay spread, Doppler spread, stationary time, were not studied. Note that in this paper, stationary time refers to the stationary interval in the time domain in order to distinguish it from stationary intervals in the space and frequency domains. Also, level crossing rate (LCR) and average fade duration (AFD) of a three dimensional (3D) unmanned aerial vehicle (UAV) channel model in the time domain were investigated in [9]. The angular spreads and delay spreads of the urban macro (UMa) channels in two typical street canyon scenarios were investigated based on extensive field measurements and modeling in [10]. The authors in [11] discussed and analyzed the channel statistical properties related to directional dispersion and spatial selectivity, such as angular PSD, angular spread, and coherence distance of wireless channel. Their relationships were also analyzed. Moreover, in [12], the authors derived and analyzed the different time-variant channel statistical properties in the high-speed train (HST) tunnel propagation scenario, such as spatial cross-correlation function (SCCF), Doppler PSD, and temporal autocorrelation function (TACF). In [13], the LCRs and AFDs of different UAV scenarios and their impact factors were studied. All these works have only studied part of the channel statistical properties in limited domains or scenarios. Besides, none of these studies has analyzed the relationships between channel parameters and channel statistical properties, except in very few cases.

The 6G pervasive channel model (6GPCM) [14] was pro-

Manuscript received November 28, 2022; revised February 24, 2023, and May 16, 2023; accepted August 10, 2023. Date of publication XX XX XXXX; date of current version XX XX XXXX. This work was supported by the National Natural Science Foundation of China (NSFC) under Grants 61960206006, the Key Technologies R&D Program of Jiangsu (Prospective and Key Technologies for Industry) under Grants BE2022067 and BE2022067-1, the Frontiers Science Center for Mobile Information Communication and Security, the EU H2020 RISE TESTBED2 project under Grant 872172, King Abdullah University of Science and Technology Research Funding under ORA-2021-CRG10-4696, and EPSRC Established Career Fellowship Prof Haas EP/R007101/1. The review of this article was coordinated by Prof. Amine Maaref.

C.-X. Wang (corresponding author) is with the National Mobile Communications Research Laboratory, School of Information Science and Engineering, Southeast University, Nanjing, 210096, China, and also with the Purple Mountain Laboratories, Nanjing, 211111, China (e-mail: chxwang@seu.edu.cn). Z. Lv is with the Purple Mountain Laboratories, Nanjing, 211111, China (e-mail: lvzhen@pmlabs.com.cn). Y. Chen is with the Department of Engineering, University of Durham, DH1 3LE, Durham, UK (e-mail: yunfei.chen@durham.ac.uk). H. Haas is with the LiFi Research and Development Center, Department Electronic and Electrical Engineering, The University of Strathclyde, Glasgow G1 1XQ, U.K. (e-mail: harald.haas@strath.ac.uk).

This is a peer-reviewed, version of record of the following paper: Wang, C-X., Lv, Z., Chen, Y., & Haas, H. (2023). A complete study of space-time-frequency statistical properties of the 6G pervasive channel model. IEEE Transactions on Communications, 71(12), 7273-7287. https://doi.org/10.1109/tcomm.2023.3307144

posed as a 3D cluster-based STF non-stationary geometry-based stochastic model (GBSM) for 6G wireless communication systems. It can be utilized to characterize wireless channels for all scenarios and all spectrum bands from sub-6 GHz to VLC [15] bands. All scenarios include global-coverage scenarios including low earth orbit (LEO) satellite, UAV, and maritime communications [16] scenarios, and full-application scenarios, such as (ultra-)massive MIMO [17], RIS [18], and industrial Internet of things (IIoT) [19] scenarios. Therefore, such a unified channel model has the capability to analyze the impacts of different frequency bands, scenarios, motions of the Tx and/or the Rx and/or scatterers, and scales of antenna arrays on channel statistical properties. However, only part of the statistical properties of the 6GPCM were studied without in-depth analysis in [14]. Also, the complicated mapping between the channel statistical properties and different frequency bands, scenarios, and system settings was not revealed.

To fill the above gap, in this paper we provide a complete study of channel statistical properties of the 6GPCM with both mathematical derivations and simulations. We classify them according to the space/time/frequency domains and relationships among their calculation methods. Also, the impacts of different frequency bands, scenarios, and system settings on statistical properties are thoroughly investigated. The novelties and main contributions of this paper are as follows:

1) We perform a comprehensive analysis of all channel statistical properties of the 6GPCM with both theoretical derivations and simulations, including STF correlation function (STFCF), SCCF, TACF, frequency correlation function (FCF), angular/Doppler/delay PSDs, root mean square (RMS) angular/Doppler/delay spreads, coherence distance/time/bandwidth, stationary distance/time/bandwidth, LCRs, and AFDs in STF domains.
2) Some theoretical/simulated key statistical properties of the 6GPCM are compared with the corresponding measurement data, including SCCF, TACF, FCF, angular/Doppler PSDs, RMS delay spread, coherence distance, and LCRs in space, time, and frequency domains.
3) The relationships between the channel model parameters and all channel statistical properties at different frequency bands in different scenarios are thoroughly investigated and revealed by both theoretical derivations and simulations.

The rest of this paper is organized as follows. In Section I, the 6GPCM [14] and its parameters are briefly reviewed. Theoretical derivations, relationships, and classifications for channel statistical properties of the 6GPCM are provided in Section II. The theoretical/simulation results are presented and compared with the corresponding measurement results in Section III. Finally, conclusions are drawn in Section IV.

The illustration of the 6GPCM is shown in Fig. 1. For clarity, the figure shows only the nth ($n = 1, ..., N_{qp}(t)$) clusters, where $N_{qp}(t)$ is the number of clusters between A_p^T and A_q^R. Here, A_p^T represents the pth antenna element of the Tx antenna array and A_q^R represents the qth antenna element of the Rx antenna array. Besides, Fig. 1 shows a multi-bounce propagation phenomenon where the nth cluster is essentially a cluster pair including the first-bounce cluster C_n^A and the last-bounce cluster C_n^Z. The propagation between C_n^A and C_n^Z is a virtual link [20]. When the delay of the virtual link is zero, C_n^A and C_n^Z become the same and the multi-bounce cluster degenerates into a single-bounce cluster. Also, there are $M_n(t)$ rays in the nth cluster at time instant t. Moreover, the dotted-line components in the figure represent movements of Tx, Rx, and clusters in the channel, since the 6GPCM supports multi-mobility. Other parameters are defined in Table I.

A. Channel Impulse Response (CIR)

The complex channel matrix of the 6GPCM can be expressed as

$$\mathbf{H} = \left[PL \cdot SH \cdot BL \cdot WE \cdot AL\right]^{1/2} \cdot \mathbf{H_s} \tag{1}$$

where PL, SH, BL, WE, and AL are path loss, shadowing, blockage loss [21], weather effect loss [22], and atmospheric gas absorption loss [23], respectively. We focus on analyzing the statistical properties of small-scale fading (SSF) in this paper. SSF in radio frequency channels can be represented as $\mathbf{H_s} = \left[h_{qp,f_c}(t,\tau)\right]_{M_R \times M_T}$, where the CIR $h_{qp,f_c}(t,\tau)$ can be calculated as

$$h_{qp,f_c}(t,\tau)=\sqrt{\frac{K(t)}{K(t)+1}}h^{\mathrm{L}}_{qp,f_c}(t,\tau)+\sqrt{\frac{1}{K(t)+1}}h^{\mathrm{N}}_{qp,f_c}(t,\tau). \tag{2}$$

Here, $K(t)$ is the Ricean K-factor at time instant t, $h^L_{qp,f_c}(t,\tau)$ and $h^N_{qp,f_c}(t,\tau)$ are the CIRs of the line-of-sight (LoS) component and the non-LoS (NLoS) component as

$$\begin{aligned} h^L_{qp,f_c}(t,\tau)=&\begin{bmatrix} F_{q,f_c,V}\left(\phi^R_{E,\mathrm{L}}(t),\phi^R_{A,\mathrm{L}}(t)\right) \\ F_{q,f_c,H}\left(\phi^R_{E,\mathrm{L}}(t),\phi^R_{A,\mathrm{L}}(t)\right)\end{bmatrix}^{\mathrm{T}}\begin{bmatrix} e^{j\theta^{VV}_{\mathrm{L}}} & 0 \\ 0 & e^{j\theta^{HH}_{\mathrm{L}}}\end{bmatrix} \\ &\mathbf{F}_{\mathrm{r}}\begin{bmatrix} F_{p,f_c,V}\left(\phi^T_{E,\mathrm{L}}(t),\phi^T_{A,\mathrm{L}}(t)\right) \\ F_{p,f_c,H}\left(\phi^T_{E,\mathrm{L}}(t),\phi^T_{A,\mathrm{L}}(t)\right)\end{bmatrix} \cdot e^{j2\pi f_c \tau^L_{qp}(t)}\delta\left(\tau-\tau^L_{qp}(t)\right) \end{aligned} \tag{3}$$

and

$$\begin{aligned} h^N_{qp,f_c}(t,\tau) = &\sum_{n=1}^{N_{qp}(t)}\sum_{m=1}^{M_n(t)}\begin{bmatrix} F_{q,f_c,V}\left(\phi^R_{E,m_n}(t),\phi^R_{A,m_n}(t)\right) \\ F_{q,f_c,H}\left(\phi^R_{E,m_n}(t),\phi^R_{A,m_n}(t)\right)\end{bmatrix}^{\mathrm{T}} \\ &\begin{bmatrix} e^{j\theta^{VV}_{mn}} & \sqrt{\mu\kappa^{-1}_{m_n}(t)}e^{j\theta^{VH}_{mn}} \\ \sqrt{\kappa^{-1}_{m_n}(t)}e^{j\theta^{HV}_{mn}} & \sqrt{\mu}e^{j\theta^{HH}_{mn}}\end{bmatrix}\mathbf{F}_{\mathrm{r}} \\ &\begin{bmatrix} F_{p,f_c,V}\left(\phi^T_{E,m_n}(t),\phi^T_{A,m_n}(t)\right) \\ F_{p,f_c,H}\left(\phi^T_{E,m_n}(t),\phi^T_{A,m_n}(t)\right)\end{bmatrix}\sqrt{P_{qp,m_n,f_c}(t)} \\ &\cdot e^{j2\pi f_c \tau_{qp,m_n}(t)} \cdot \delta\left(\tau-\tau_{qp,m_n}(t)\right). \end{aligned} \tag{4}$$

In (3) and (4), $\{\cdot\}^{\mathrm{T}}$ denotes the transposition operation, $F_{p(q),f_c,V}$ and $F_{p(q),f_c,H}$ stand for the antenna patterns. Also, $\kappa_{m_n}(t)$ and μ are the cross polarization power ratio and the co-polar imbalance [8], respectively. In addition, $\theta^{VV}_{m_n}$, $\theta^{VH}_{m_n}$, $\theta^{HV}_{m_n}$, $\theta^{HH}_{m_n}$, θ^{VV}_{L} and θ^{HH}_{L} are the initial phases, which are random variables uniformly distributed over $(0, 2\pi]$. Moreover, $\mathbf{F}_{\mathrm{r}}$ represents Faraday rotation matrix in a LEO satellite scenario [24]. In the derivations of channel statistical properties, we set $\mathbf{F}_{\mathrm{r}} = 1$. Additionally, $P_{qp,m_n,f_c}(t)$ and $\tau_{qp,m_n}(t)$ are

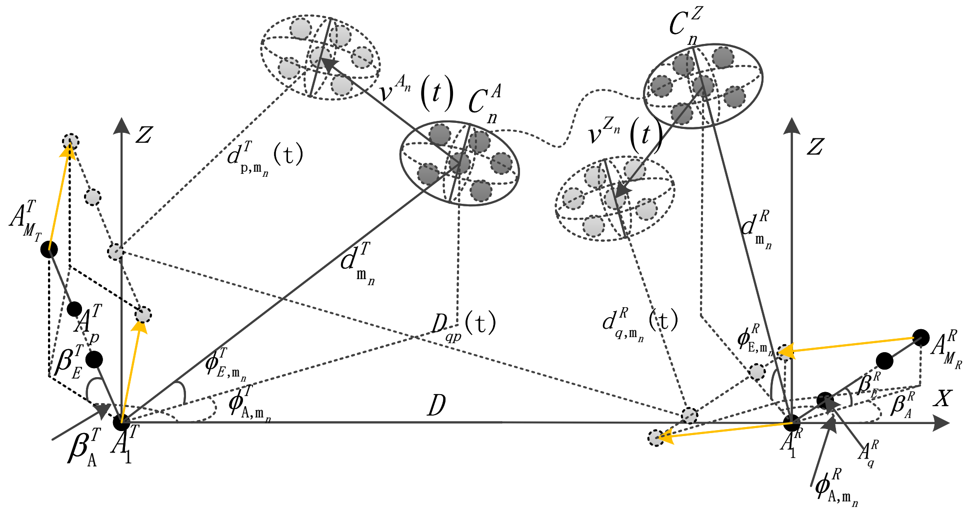

Fig. 1. Illustration of the 6GPCM [14].

TABLE I
DEFINITIONS OF MAIN CHANNEL PARAMETERS [14].

Parameter	**Definition**
M_T/M_R	The number of antenna elements of the Tx/Rx antenna array
A^T_p/A^R_q	The pth/qth antenna element of the Tx/Rx antenna array
δ^T_p/δ^R_q	Antenna element spacing between A^T_p/A^R_q to A^T_1/A^R_1
$\vec{A}^T_p/\vec{A}^R_q$	Coordinate of A^T_p/A^R_q in global coordinate
$\vec{C}^A_n/\vec{C}^Z_n$	Coordinate of center of C^A_n/C^Z_n relative to reference antenna element $\vec{A}^T_1/\vec{A}^R_1$
$\vec{C}^A_{m_n}/\vec{C}^Z_{m_n}$	Coordinate of mth scatterer in C^A_n/C^Z_n relative to reference antenna element $\vec{A}^T_1/\vec{A}^R_1$
β^T_A/β^T_E	The azimuth angle/the elevation angle of the Tx antenna array
β^R_A/β^R_E	The azimuth angle/the elevation angle of the Rx antenna array
$\phi^T_{A,m_n}(t)$	Azimuth angle of departure (AoD) of $C^A_{m_n}$ at t
$\phi^T_{E,m_n}(t)$	Elevation AoD of $C^A_{m_n}$ at t
$\phi^R_{A,m_n}(t)$	Azimuth angle of arrival (AoA) of $C^Z_{m_n}$ at t
$\phi^R_{E,m_n}(t)$	Elevation AoA of $C^Z_{m_n}$ at t
$\alpha^T(R)_A(t)/\alpha^T(R)_E(t)$	Azimuth/elevation angle of moving direction of the Tx (Rx) antenna array at t
$\alpha^{A_n}_A(t)/\alpha^{A_n}_E(t)$	Azimuth/elevation angle of moving direction of C^A_n at t
$\vec{v}^T(t)/\vec{v}^R(t)$	Moving speed vector of the Tx/Rx antenna array at t
$\vec{v}^{A_n}(t)/\vec{v}^{Z_n}(t)$	Moving speed vector of C^A_n/C^Z_n at t
D	Distance between antenna elements A^T_1 and A^R_1 at initial time
$D_{qp}(t)$	Distance between antenna elements A^T_p and A^R_q at t
$\hat{d}^T_{p,\,m_n}(t)/\hat{d}^R_{q,\,m_n}(t)$	Unit vector between A^T_p and $C^A_{m_n}/A^R_q$ and $C^Z_{m_n}$ at t

the time-varying power and delay of the mth ray in the nth path between A^T_p and A^R_q, respectively. In multi-bounce paths, $\tau_{qp,m_n}(t) = (d^T_{m_n}(t) + d^R_{m_n}(t))/c + \tilde{\tau}_{m_n}(t)$, where $\tilde{\tau}_{m_n}$ is the delay of the virtual link between $C^A_{m_n}$ and $C^Z_{m_n}$. Also, $\tau^L_{qp}(t)$ is the LoS-path time delay at time t, which can be calculated as $\tau^L_{qp}(t) = D_{qp}(t)/c$, where c is the speed of light. Then we can calculate the power $P_{qp,m_n,f_c}(t)$ using the delay [14].

For the positions of scatterers, they are modeled by the ellipsoid Gaussian scattering distribution [8] in 6GPCM. In this model, distributions of scatterers centering $(\bar{d}^X_n, \bar{\phi}^X_{E,n}, \bar{\phi}^X_{A,n})$ in the nth cluster on three axes follow three independent Gaussian distributions with standard deviation of σ^T_x (σ^R_x), σ^T_y (σ^R_y), and σ^T_z (σ^R_z) at the Tx (Rx) side, respectively. Then, we can obtain $\vec{C}^A_{m_n} = \left(d^T_{m_n}, \phi^T_{A,m_n}, \phi^T_{E,m_n}\right)$ and $\vec{C}^Z_{m_n} = \left(d^R_{m_n}, \phi^R_{A,m_n}, \phi^R_{E,m_n}\right)$. Here, $d^T_{m_n}/d^R_{m_n}$, $\phi^T_{A,m_n}/\phi^R_{A,m_n}$, and $\phi^T_{E,m_n}/\phi^R_{E,m_n}$ are the distance, azimuth angle, and elevation angle of the mth ray in the nth cluster relative to $\vec{A}^T_1/\vec{A}^R_1$, respectively.

Using the geographical positions of Tx, Rx, and scatterers, the delays, angles, and powers of the rays in the clusters can be obtained. For convenience, we have omitted the time variable t, but note that these variables are all time-varying. Furthermore, the 6GPCM supports birth-death processes of clusters in STF domains [14]. The number of clusters at time instant t can be calculated as

$$N(t) = N_{\text{surv}}(t) + N_{\text{new}}(t) \tag{5}$$

where $N_{\text{surv}}(t)$ is the number of survived clusters at time instant t. It is determined by the survival probability $P_{\text{surv}}\left(\delta_p, \delta_q, \Delta t_{\text{BD}}, \Delta f_{\text{BD}}\right)$, given by

$$\begin{aligned} & P_{\text{surv}}\left(\delta_p, \delta_q, \Delta t_{\text{BD}}, \Delta f_{\text{BD}}\right) \\ & \quad = P_{\text{surv}}^{T}\left(\Delta t_{\text{BD}}, \delta_p\right) P_{\text{surv}}^{R}\left(\Delta t_{\text{BD}}, \delta_q\right) P_{\text{surv}}\left(\Delta f_{\text{BD}}\right). \end{aligned} \tag{6}$$

Here, Δt_{BD} and Δf_{BD} are integer multiples of Δt and Δf, respectively. Calculations and typical values of (6) can be found in [25], [26]. Additionally, $N_{\text{new}}(t)$ is the newly generated clusters at time instant t. It follows the Poisson distribution with mean value $\mathrm{E}\left(N_{\text{new}}\right)$, given by

$$\mathrm{E}\left(N_{\text{new}}\right) = \frac{\lambda_G}{\lambda_R}\left(1 - P_{\text{surv}}\left(\delta_p, \delta_q, \Delta t_{\text{BD}}, \Delta f_{\text{BD}}\right)\right) \tag{7}$$

where λ_G is the generation (birth) rate of clusters and λ_R is the recombination (death) rate of clusters. Their typical values can be found in [8].

B. *Channel Transfer Function (CTF)*

We can get the CTF by taking the Fourier transform of the CIR in (2) over τ as

$$H_{qp,f_c}(t,f) = \sqrt{\frac{K(t)}{K(t)+1}} H_{qp,f_c}^{L}(t,f) + \sqrt{\frac{1}{K(t)+1}} H_{qp,f_c}^{N}(t,f) \tag{8}$$

where $H_{qp,f_c}^{L}(t,f)$ is

$$\begin{aligned} H_{qp,f_c}^{L}(t,f) = & \begin{bmatrix} F_{q,f_c,V}\left(\phi_{E,\mathrm{L}}^{R}(t), \phi_{A,\mathrm{L}}^{R}(t)\right) \\ F_{q,f_c,H}\left(\phi_{E,\mathrm{L}}^{R}(t), \phi_{A,\mathrm{L}}^{R}(t)\right) \end{bmatrix}^{\mathrm{T}} \begin{bmatrix} e^{j\theta_{\mathrm{L}}^{VV}} & 0 \\ 0 & e^{j\theta_{\mathrm{L}}^{HH}} \end{bmatrix} \\ & \mathbf{F}_{\mathrm{r}} \begin{bmatrix} F_{p,f_c,V}\left(\phi_{E,\mathrm{L}}^{T}(t), \phi_{A,\mathrm{L}}^{T}(t)\right) \\ F_{p,f_c,H}\left(\phi_{E,\mathrm{L}}^{T}(t), \phi_{A,\mathrm{L}}^{T}(t)\right) \end{bmatrix} \cdot e^{j2\pi(f_c - f)\tau_{qp}^{L}(t)} \end{aligned} \tag{9}$$

and $H_{qp,f_c}^{N}(t,f)$ is

$$\begin{aligned} H_{qp,f_c}^{N}(t,f) = & \sum_{n=1}^{N_{qp}(t)} \sum_{m=1}^{M_n(t)} \begin{bmatrix} F_{q,f_c,V}\left(\phi_{E,m_n}^{R}(t), \phi_{A,m_n}^{R}(t)\right) \\ F_{q,f_c,H}\left(\phi_{E,m_n}^{R}(t), \phi_{A,m_n}^{R}(t)\right) \end{bmatrix}^{\mathrm{T}} \\ & \begin{bmatrix} e^{j\theta_{mn}^{VV}} & \sqrt{\mu\kappa_{m_n}^{-1}(t)} e^{j\theta_{mn}^{VH}} \\ \sqrt{\kappa_{m_n}^{-1}(t)} e^{j\theta_{mn}^{HV}} & \sqrt{\mu} e^{j\theta_{mn}^{HH}} \end{bmatrix} \mathbf{F}_{\mathrm{r}} \\ & \begin{bmatrix} F_{p,f_c,V}\left(\phi_{E,m_n}^{T}(t), \phi_{A,m_n}^{T}(t)\right) \\ F_{p,f_c,H}\left(\phi_{E,m_n}^{T}(t), \phi_{A,m_n}^{T}(t)\right) \end{bmatrix} \sqrt{P_{qp,m_n f_c}(t)} \\ & \cdot e^{j2\pi(f_c - f)\tau_{qp,m_n}(t)}. \end{aligned} \tag{10}$$

Note that, when large bandwidth in the millimeter wave (mmWave) or THz bands is used, we need to multiply the power by $\left(\frac{f}{f_c}\right)^{\gamma_{m_n}}$ to mimic the frequency-dependent property in the frequency domain, where γ_{m_n} is the frequency-dependent factor [27].

II. STATISTICAL PROPERTIES OF THE 6GPCM

In general, we introduce channel statistical properties in the sequence of space/angle domain, time/Doppler frequency domain, and frequency/delay domain. This section is divided into six sub-sections from Section III-A to Section III-F corresponding to six red dashed line boxes in Fig. 2, respectively. Firstly, we can get the STF non-stationary CF using the CTFs of channels in Section III-A. Then, space- or time- or frequency-domain correlation function can be obtained from the general STF non-stationary CF by imposing the intervals in the other two domains to 0. Afterwards, the PSDs, RMS spreads, and coherence variables can be calculated from the CFs for different domains. These statistical properties in different domains are described in Section III-B, Section III-C, and Section III-D, respectively. In order to understand the stationarity regions, stationary distance/time/bandwidth are investigated in Section III-E. In addition, we can obtain the amplitude probability density function (PDF) and phase PDF using the CTF of the channel. Finally, in Section III-F we study LCRs and corresponding AFDs in space, time, and frequency domains based on their amplitude PDF and the joint PDF of the amplitude and the amplitude slope.

A. *STF Non-stationary CF*

STF non-stationary CF measures the correlation between two channels at different time instants and different frequencies between different antenna elements. The STF non-stationary CF between $H_{qp}(t,f)$ and $H_{\tilde{q}\tilde{p}}(t+\Delta t, f+\Delta f)$ is defined as

$$\begin{aligned} & R_{qp,\tilde{q}\tilde{p}}\left(t, f; \Delta r^{T}, \Delta r^{R}, \Delta t, \Delta f\right) \\ & \quad = \mathrm{E}\left[H_{qp}(t,f) H_{\tilde{q}\tilde{p}}^{*}(t+\Delta t, f+\Delta f)\right] \end{aligned} \tag{11}$$

where $\mathrm{E}[\cdot]$ is the statistical average, $(\cdot)^{*}$ is the complex conjugation operation, Δr^{T} is the antenna element spacing between A_p^T to $A_{\tilde{p}}^T$ and Δr^{R} is the antenna element spacing between A_q^R to $A_{\tilde{q}}^R$, as $\Delta r^{T} = \delta_{\tilde{p}} - \delta_p$ and $\Delta r^{R} = \delta_{\tilde{q}} - \delta_q$. By substituting (8) into (11), the STF non-stationary CF can be rewritten as

$$\begin{aligned} & R_{qp,\tilde{q}\tilde{p}}\left(t, f; \Delta r^{T}, \Delta r^{R}, \Delta t, \Delta f\right) \\ & = \sqrt{\frac{K(t)}{K(t)+1} \cdot \frac{K(t+\Delta t)}{K(t+\Delta t)+1}} R_{qp,\tilde{q}\tilde{p}}^{L}\left(t, f; \Delta r^{T}, \Delta r^{R}, \Delta t, \Delta f\right) \\ & + \sqrt{\frac{1}{K(t)+1} \cdot \frac{1}{K(t+\Delta t)+1}} R_{qp,\tilde{q}\tilde{p}}^{N}\left(t, f; \Delta r^{T}, \Delta r^{R}, \Delta t, \Delta f\right) \end{aligned} \tag{12}$$

where $R_{qp,\tilde{q}\tilde{p}}^{L}\left(t, f; \Delta r^{T}, \Delta r^{R}, \Delta t, \Delta f\right)$ is the STF non-stationary CF of LoS component. It can be calculated as

$$\begin{aligned} & R_{qp,\tilde{q}\tilde{p}}^{L}\left(t, f; \Delta r^{T}, \Delta r^{R}, \Delta t, \Delta f\right) \\ & = E\left[H_{qp,f_c}^{L}(t,f) H_{\tilde{q}\tilde{p},f_c}^{*L}(t+\Delta t, f+\Delta f)\right] \\ & = e^{j2\pi \frac{(f_c - f)\left(d_{qp}(t) - d_{\tilde{q}\tilde{p}}(t+\Delta t)\right)}{\lambda f_c} - j2\pi\Delta f \frac{d_{\tilde{q}\tilde{p}}(t+\Delta t)}{\lambda f_c}} \end{aligned} \tag{13}$$

where $d_{qp}(t)/d_{\tilde{q}\tilde{p}}(t)$ represents the travel distance from $A_p^T/A_{\tilde{p}}^T$ to $A_q^R/A_{\tilde{q}}^R$ of the LoS component. However, the calculation is complicated and the details can be referred to [14].

Also, $R_{qp,\tilde{q}\tilde{p}}^{N}\left(t, f; \Delta r^{T}, \Delta r^{R}, \Delta t, \Delta f\right)$ is the STF non-

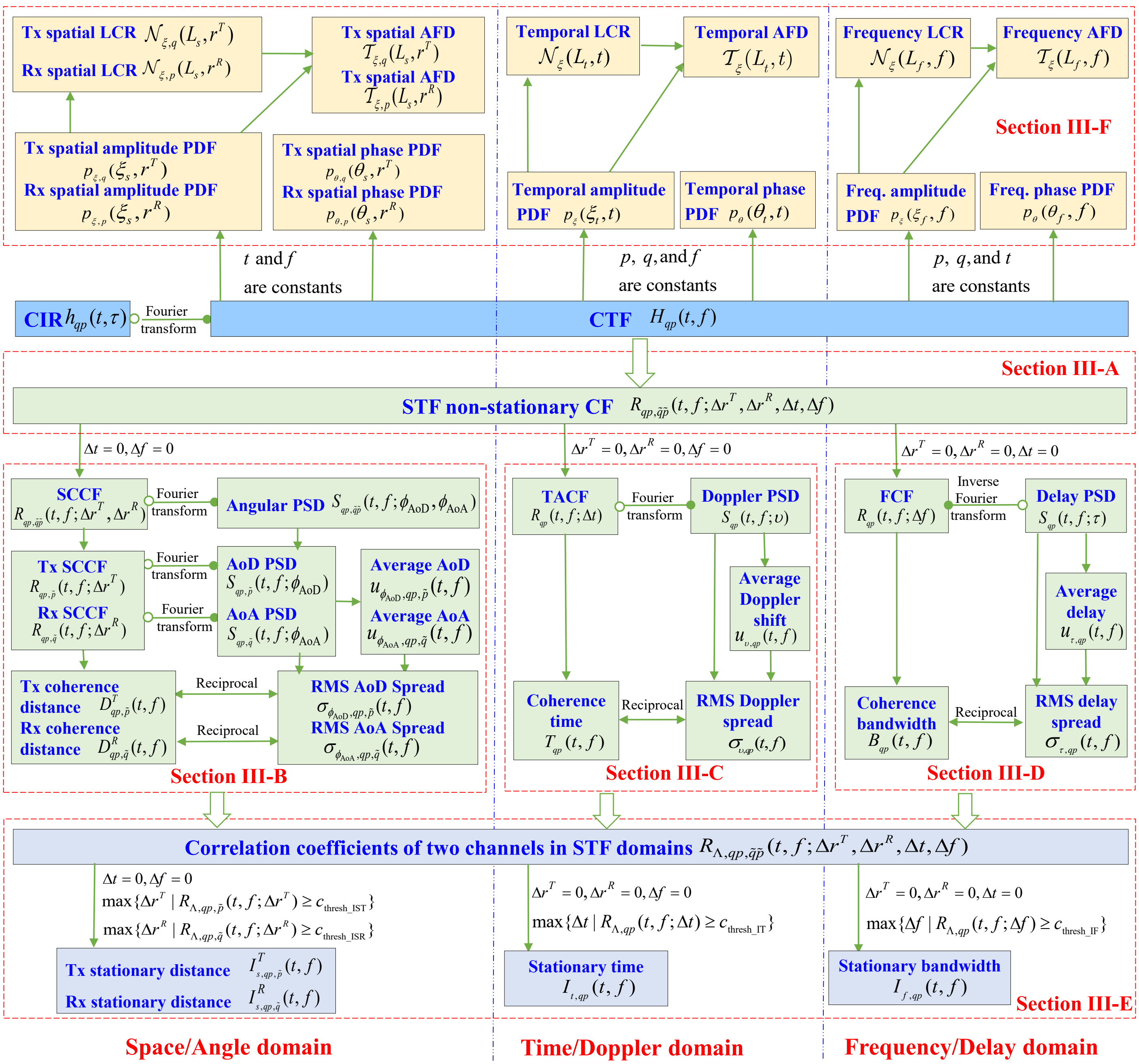

Fig. 2. Relationships and classifications of channel statistical properties.

stationary CF of NLoS components. It can be calculated as

$$\begin{aligned}
&R^N_{qp,\tilde{q}\tilde{p}}\left(t,f;\Delta r^T,\Delta r^R,\Delta t,\Delta f\right)\\
&=E\left[H^N_{qp,f_c}\left(t,f\right)H^{*N}_{\tilde{q}\tilde{p},f_c}\left(t{+}\Delta t,f{+}\Delta f\right)\right]\\
&=P_{\text{surv}}\!\left(\Delta r^T\!,\Delta r^R\!,\Delta t,\Delta f\right)E\left[\sum_{n=1}^{N_{qp}(t)}\sum_{m=1}^{M_n(t)}\sqrt{P_{qp,m_n}\left(t,f\right)}\right.\\
&\sqrt{P_{\tilde{q}\tilde{p},m_n}\left(t+\Delta t,f+\Delta f\right)}\\
&\left.\cdot\, e^{j2\pi(f_c-f)\frac{d_{qp,m_n}(t)-d_{\tilde{q}\tilde{p},m_n}(t+\Delta t)}{\lambda f_c}-j2\pi\Delta f\frac{d_{\tilde{q}\tilde{p},m_n}(t+\Delta t)}{\lambda f_c}}\right]. \qquad (14)
\end{aligned}$$

Similarly, calculations of $d_{qp,m_n}(t)$ and $d_{\tilde{q}\tilde{p},m_n}(t)$ of NLoS components can be referred to [14].

A channel is STF non-stationary if the STFCF is not only a function of Δr^T, Δr^R, Δt, and Δf, but also relies on the antenna element indexes p/q, time instant t, and frequency point f. As shown in Fig. 3, when the channel is wide-sense stationary (WSS) in the space domain, the space WSS STFCF can be written as $R(t,f;\Delta r^T,\Delta r^R,\Delta t,\Delta f)$. When the channel is WSS in the time domain, the time WSS STFCF can be written as $R_{qp,\tilde{q}\tilde{p}}(f;\Delta r^T,\Delta r^R,\Delta t,\Delta f)$. Also, when the channel is WSS in the frequency domain, the frequency WSS STFCF can be written as $R_{qp,\tilde{q}\tilde{p}}(t;\Delta r^T,\Delta r^R,\Delta t,\Delta f)$. In addition, we can further assume that the channel is WSS in two domains, or in other words the channel is non-stationary in the

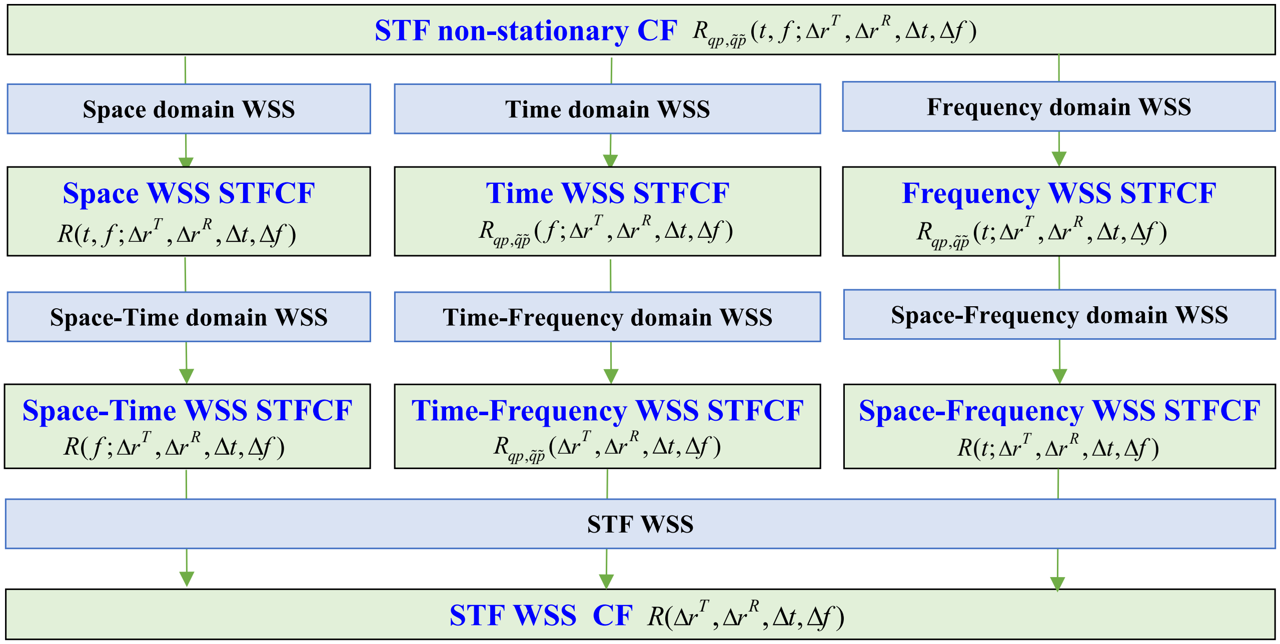

Fig. 3. STFCFs under different stationary conditions.

third domain. For example, if the channel is WSS in the space-time domains, the space-time WSS STFCF can be written as $R(f;\Delta r^T,\Delta r^R,\Delta t,\Delta f)$. If the channel is WSS in the time-frequency domains, the time-frequency WSS STFCF can be written as $R_{qp,\tilde{q}\tilde{p}}(\Delta r^T,\Delta r^R,\Delta t,\Delta f)$. Also, if the channel is WSS in the space-frequency domains, the space-frequency WSS STFCF can be written as $R(t;\Delta r^T,\Delta r^R,\Delta t,\Delta f)$. Finally, if the channel is WSS in the STF domains, the STFCF can be written as $R(\Delta r^T,\Delta r^R,\Delta t,\Delta f)$. In the following subsections, unless otherwise specified, we assume that the channel is non-stationary in the STF domains.

B. SCCF, Coherence Distance, Angular PSD, and RMS Angular Spread

1) SCCF: The STF non-stationary CF can be decomposed into SCCF $R_{qp,\tilde{q}\tilde{p}}\left(t,f;\Delta r^T,\Delta r^R\right)$ by setting $\Delta t=0$ and $\Delta f=0$. It is important to mention that use the same transmitting antenna element A_p^T, i.e., $\Delta r^T=0$, resulting in the SCCF $R_{qp,\tilde{q}}\left(t,f;\Delta r^R\right)$ at the Rx side. Also, use the same receiving antenna element A_q^R, i.e., $\Delta r^R=0$, resulting in the SCCF $R_{qp,\tilde{p}}\left(t,f;\Delta r^T\right)$ at the Tx side. Here, SCCF at the Tx side $R_{qp,\tilde{p}}\left(t,f;\Delta r^T\right)$ is used by setting $\Delta t=0$, $\Delta f=0$, $q=\tilde{q}$, and $\Delta r^R=0$ in (11) as an example for analysis. It can be obtained as

$$
\begin{aligned}
&R_{qp,\tilde{p}}\left(t,f;\Delta r^T\right)=E\left[H_{qp}\left(t,f\right)H_{q\tilde{p}}^*\left(t,f\right)\right]\\
&=\frac{K\left(t\right)}{K\left(t\right)+1}R_{qp,\tilde{p}}^L\left(t,f;\Delta r^T\right)+\frac{1}{K\left(t\right)+1}R_{qp,\tilde{p}}^N\left(t,f;\Delta r^T\right)\\
&=\frac{K\left(t\right)}{K\left(t\right)+1}e^{j2\pi\frac{(f_c-f)\left(d_{qp}(t)-d_{q\tilde{p}}(t)\right)}{\lambda f_c}}+\frac{1}{K\left(t\right)+1}P_{\text{surv}}\left(\Delta r^T\right)\\
&E\left[\sum_{n=1}^{N_{qp}(t)}\sum_{m=1}^{M_n(t)}\sqrt{P_{qp,m_n}\left(t,f\right)}\sqrt{P_{q\tilde{p},m_n}\left(t,f\right)}\right.\\
&\left.e^{j2\pi\frac{(f_c-f)\left(d_{qp,m_n}(t)-d_{q\tilde{p},m_n}(t)\right)}{\lambda f_c}}\right]. \qquad (15)
\end{aligned}
$$

Following some simplifications [8] and assuming that the environment is static, $d_{qp,m_n}(t)-d_{q\tilde{p},m_n}(t)$ can be obtained as

$$
\begin{aligned}
&d_{qp,m_n}(t)-d_{q\tilde{p},m_n}(t)\\
&=\cos(\vartheta^T)(\delta_{\tilde{p}}-\delta_p)+\sin^2(\vartheta^T)(\delta_p^2-\delta_{\tilde{p}}^2)/(2d_{p,m_n}^T) \qquad (16)
\end{aligned}
$$

where ϑ^T is the angle between the Tx and the departure wave of $C_{m_n}^A$. It is determined by

$$
\begin{aligned}
\cos(\vartheta^T)&=\cos(\phi_{E,m_n}^T)\cos(\beta_E^T)\cos(\beta_A^T-\phi_{A,m_n}^T)\\
&+\sin(\phi_{E,m_n}^T)\sin(\beta_E^T). \qquad (17)
\end{aligned}
$$

Similarly, the SCCF observed at the Rx side $R_{qp,\tilde{q}}\left(t,f;\Delta r^R\right)$ can also be obtained.

2) Coherence Distance: The coherence distance on the antenna array axis is the minimum antenna element spacing within which the SCCF equals to the threshold $c_{\text{thresh\_D}}\in[0,1]$. The Tx-side coherence distance is defined as

$$
D_{qp,\tilde{p}}^T(t,f)=\min\left\{\Delta r^T>0:R_{qp,\tilde{p}}\left(t,f;\Delta r^T\right)=c_{\text{thresh\_D}}\right\}. \qquad (18)
$$

Similarly, the Rx-side coherence distance $D_{qp,\tilde{q}}^R(t,f)$ based on the Rx-side SCCF $R_{qp,\tilde{q}}\left(t,f;\Delta r^R\right)$ can also be obtained.

3) Angular PSD: Spatial-Doppler PSD $S_{qp,\tilde{q}\tilde{p}}\left(t,f;\varpi^T,\varpi^R\right)$ is defined as the Fourier transform of SCCF $R_{qp,\tilde{q}\tilde{p}}\left(t,f;\Delta r^T,\Delta r^R\right)$ with respect to (w.r.t.) the interval Δr^T and Δr^R. Here, spatial-Doppler PSDs at the Tx and Rx sides, i.e., $S_{qp,\tilde{p}}\left(t,f;\varpi^T\right)$ and $S_{qp,\tilde{q}}\left(t,f;\varpi^R\right)$, can be obtained as

$$
S_{qp,\tilde{p}}\left(t,f;\varpi^T\right)=\int R_{qp,\tilde{p}}\left(t,f;\Delta r^T\right)e^{-j2\pi\varpi^T\Delta r^T}d\Delta r^T \qquad (19)
$$

$$S_{qp,\tilde{q}}\left(t,f;\varpi^R\right)=\int R_{qp,\tilde{q}}\left(t,f;\Delta r^R\right)e^{-j2\pi\varpi^R\Delta r^R}d\Delta r^R \tag{20}$$

where ϖ^T (ϖ^R) is the spatial-Doppler frequency variable. In the above expressions, $\varpi^{T(R)}$ is defined as $\varpi^{T(R)}=\Omega^{T(R)}\cdot\beta^{T(R)}$, where $\Omega^{T(R)}$ is the unit vector of the AoD (AoA) wave and $\beta^{T(R)}$ is the orientation of the antenna array at the Tx (Rx) side [11]. Notice that, if $\vartheta^{T(R)}$ is the angle between $\Omega^{T(R)}$ and $\beta^{T(R)}$, then $\varpi^{T(R)}=\cos(\vartheta^{T(R)})$ [11]. Consequently, the angular PSD $S_{qp,\tilde{q}\tilde{p}}\left(t,f;\phi_{\text{AoD}},\phi_{\text{AoA}}\right)$ can be obtained from the spatial-Doppler PSD $S_{qp,\tilde{q}\tilde{p}}\left(t,f;\varpi^T,\varpi^R\right)$ using the coordinate transformation between $\phi_{\text{AoD (AoA)}}$ and $\varpi^{T(R)}$. Also, the AoD PSD is $S_{qp,\tilde{p}}\left(t,f;\phi_{\text{AoD}}\right)$ and AoA PSD is $S_{qp,\tilde{q}}\left(t,f;\phi_{\text{AoA}}\right)$.

4) RMS Angular Spread: The RMS angular spread at the Tx side, which is the AoD spread, is the square root of the second-order central moment of angular PSD at the corresponding side, defined as

$$\begin{aligned}&\sigma_{\phi_{\text{AoD}},qp,\tilde{p}}\left(t,f\right)\\&=\sqrt{\frac{\int_0^{2\pi}(\phi_{\text{AoD}}-u_{\phi_{\text{AoD}},qp,\tilde{p}}\left(t,f\right))^2 S_{qp,\tilde{p}}\left(t,f;\phi_{\text{AoD}}\right)d\phi_{\text{AoD}}}{\int_0^{2\pi}S_{qp,\tilde{p}}\left(t,f;\phi_{\text{AoD}}\right)d\phi_{\text{AoD}}}}\end{aligned} \tag{21}$$

where $S_{qp,\tilde{p}}\left(t,f;\phi_{\text{AoD}}\right)$ is the Tx-side AoD PSD. Here, $u_{\phi_{\text{AoD}},qp,\tilde{p}}\left(t,f\right)$ is the average AoD and is also the first-order moment of Tx-side AoD PSD. In the same way, we can get the average AoA $u_{\phi_{\text{AoA}},qp,\tilde{q}}\left(t,f\right)$ and the Rx-side RMS AoA spread $\sigma_{\phi_{\text{AoA}},qp,\tilde{q}}\left(t,f\right)$, which are the first-order moment and the square root of the second-order central moment of Rx-side AoA PSD $S_{qp,\tilde{q}}\left(t,f;\phi_{\text{AoA}}\right)$.

C. TACF, Coherence Time, Doppler PSD, and RMS Doppler Spread

1) TACF: TACF measures the time correlation of the channel. Let $\Delta r^T=0,\Delta r^R=0$, and $\Delta f=0$, i.e., using the same antenna elements at both Tx and Rx sides, in (11), we can obtain the TACF $R_{qp}\left(t,f;\Delta t\right)$ as

$$\begin{aligned}R_{qp}\left(t,f;\Delta t\right)&=E\left[H_{qp,f_c}\left(t,f\right)H^*_{qp,f_c}\left(t+\Delta t\right)\right]\\&=\sqrt{\frac{K(t)}{K(t)+1}\cdot\frac{K(t{+}\Delta t)}{K(t{+}\Delta t){+}1}}R^L_{qp}\left(t,f;\Delta t\right)+\\&\sqrt{\frac{1}{K(t){+}1}\cdot\frac{1}{K(t{+}\Delta t){+}1}}R^N_{qp}\left(t,f;\Delta t\right).\end{aligned} \tag{22}$$

Here, $R^L_{qp}\left(t,f;\Delta t\right)$ is the TACF of the LoS component and is given by

$$R^L_{qp}\left(t,f;\Delta t\right)=e^{j2\pi\frac{(f_c-f)\left(d_{qp}(t)-d_{qp}(t+\Delta t)\right)}{\lambda f_c}}. \tag{23}$$

Also, the TACF of the NLoS component $R^N_{qp}\left(t,f;\Delta t\right)$ can be calculated as

$$\begin{aligned}R^N_{qp}\left(t,f;\Delta t\right)=P_{\text{surv}}\left(\Delta t\right)E&\left[\sum_{n=1}^{N_{qp}(t)}\sum_{m=1}^{M_n(t)}\sqrt{P_{qp,m_n}\left(t,f\right)}\right.\\&\left.\sqrt{P_{qp,m_n}\left(t+\Delta t,f\right)}\cdot e^{j2\pi(f_c-f)\frac{d_{qp,m_n}(t)-d_{qp,m_n}(t+\Delta t)}{\lambda f_c}}\right]\end{aligned} \tag{24}$$

where $d_{qp,m_n}\left(t\right)-d_{qp,m_n}\left(t+\Delta t\right)$ in (24) can be approximated as

$$d_{qp,m_n}(t)-d_{qp,m_n}\left(t+\Delta t\right)=-||\vec{v}^T+\vec{v}^{A_n}+\vec{v}^R+\vec{v}^{Z_n}||\Delta t. \tag{25}$$

2) Coherence Time: Coherence time is the minimum time interval that fulfils the condition that the TACF equals to the threshold $c_{\text{thresh\_T}}\in[0,1]$, as

$$T_{qp}(t,f)=\min\left\{\Delta t>0:R_{qp}\left(t,f;\Delta t\right)=c_{\text{thresh\_T}}\right\}. \tag{26}$$

3) Doppler PSD: Doppler PSD, which measures the power distribution over the Doppler frequency axis, is the Fourier transform of TACF $R_{qp}\left(t,f;\Delta t\right)$ w.r.t. the time interval Δt. It can be calculated as

$$S_{qp}\left(t,f;\upsilon\right)=\int R_{qp}\left(t,f;\Delta t\right)e^{-j2\pi\upsilon\Delta t}d\Delta t \tag{27}$$

where υ is the Doppler frequency. Besides, the time-varying Doppler frequency of the mth ray in the nth cluster from A^T_p to A^R_q at t can be calculated [14] as

$$\begin{aligned}&\upsilon_{qp,m_n(t)}=\\&\frac{\left(\vec{v}^T(t)-\vec{v}^{A_n}(t)\right)\cdot\hat{d}^T_{p,m_n}(t)+\left(\vec{v}^R(t)-\vec{v}^{Z_n}(t)\right)\cdot\hat{d}^R_{q,m_n}(t)}{c/f_c}.\end{aligned} \tag{28}$$

4) RMS Doppler Spread: The motions of Tx, Rx, and scatterers in the channel cause the channel dispersion in the Doppler frequency domain, and the multipath propagation causes channel dispersions in the time and angular domains. RMS Doppler spread, RMS delay spread, and RMS angular spread are often used to measure these dispersions. RMS Doppler spread can be calculated as the square root of the second-order central moment of Doppler PSD, as

$$\sigma_{\upsilon,qp}\left(t,f\right)=\sqrt{\frac{\int_0^{\infty}(\upsilon-u_{\upsilon,qp}\left(t,f\right))^2 S_{qp}\left(t,f;\upsilon\right)d\upsilon}{\int_0^{\infty}S_{qp}\left(t,f;\upsilon\right)d\upsilon}} \tag{29}$$

where $u_{\upsilon,qp}\left(t,f\right)$ is the average Doppler shift and is also the first-order moment of the Doppler PSD. Since the value of coherence time is the reciprocal of the value of the RMS Doppler spread [28], we only use one of them as an example to analyze the impact of coherence time and RMS Doppler spread. Similarly, the coherence distance and RMS angular spread are a pair, so are the coherence bandwidth and RMS delay spread. Consequently, we only analyze the impact of RMS Doppler spread, RMS Delay spread, and RMS angular spread in Section III.

D. FCF, Coherence Bandwidth, Delay PSD, and RMS Delay Spread

1) FCF: FCF measures the frequency correlation of the channel. We can reduce the STF non-stationary CF to FCF $R_{qp}\left(t,f;\Delta f\right)$ by setting $\Delta r^T=0$, $\Delta r^R=0$, and $\Delta t=0$ in (11) as

$$\begin{aligned}&R_{qp}\left(t,f;\Delta f\right)=E\left[H_{qp}\left(t,f\right)H_{qp}^{*}\left(f+\Delta f\right)\right]\\&=\frac{K\left(t\right)}{K\left(t\right)+1}R_{qp}^{L}\left(t,f;\Delta f\right)+\frac{1}{K\left(t\right)+1}R_{qp}^{N}\left(t,f;\Delta f\right)\\&=\frac{K\left(t\right)}{K\left(t\right)+1}e^{-j2\pi\frac{\Delta f\, d_{qp}(t)}{\lambda f_c}}+\frac{1}{K\left(t\right)+1}P_{\text{surv}}\left(\Delta f\right)\\&E\left[\sum_{n=1}^{N_{qp}(t)}\sum_{m=1}^{M_n(t)}\sqrt{P_{qp,m_n}(t,f)}\sqrt{P_{qp,m_n}(t,f+\Delta f)}e^{-j2\pi\Delta f\frac{d_{qp,m_n}(t)}{\lambda f_c}}\right].\end{aligned}\tag{30}$$

2) Coherence Bandwidth: The coherence bandwidth is the minimum frequency intervals that fulfills the condition that the FCF of a channel equals to the threshold $c_{\text{thresh\_B}}\in[0,1]$. It can be written as

$$B_{qp}(t,f)=\min\left\{\Delta f>0:R_{qp}\left(t,f;\Delta f\right)=c_{\text{thresh\_B}}\right\}.\tag{31}$$

3) Delay PSD: Delay PSD gives the channel PSD as a function of the time delay τ. Also, it is the inverse Fourier transform of FCF $R_{qp}\left(t,f;\Delta f\right)$ w.r.t. Δf. It can be obtained as

$$S_{qp}\left(t,f;\tau\right)=\int R_{qp}\left(t,f;\Delta f\right)e^{j2\pi\tau\Delta f}d\Delta f.\tag{32}$$

This can be calculated as

$$S_{qp}\left(t,f;\tau\right)=\sum_{n=1}^{N_{qp}(t)}\sum_{m=1}^{M_n(t)}P_{qp,m_n}(t,f)\delta\left(\tau-\tau_{qp,m_n}(t)\right).\tag{33}$$

Note that the two expressions of delay PSD can be derived from each other. Here, $P_{qp,m_n}(t,f)$ is affected by the STF evolution of the clusters in space, time, and frequency domains, and will further affect the delay PSD.

4) RMS Delay Spread: Similar to the RMS Doppler spread, the RMS delay spread is defined as the square root of the second-order central moment of the delay PSD. It can be calculated as

$$\sigma_{\tau,qp}\left(t,f\right)=\sqrt{\frac{\int_{0}^{\infty}(\tau-u_{\tau,qp}\left(t,f\right))^2S_{qp}\left(t,f;\tau\right)d\tau}{\int_{0}^{\infty}S_{qp}\left(t,f;\tau\right)d\tau}}\tag{34}$$

where $u_{\tau,qp}\left(t,f\right)$ is the average delay and is also the first-order moment of the delay PSD.

E. Stationary Distance/Time/Bandwidth

The stationary time is the maximum time duration during which the channel can be seen as a WSS channel in the time domain. We can use several methods to calculate the stationary time, such as correlation matrix distance (CMD) [29], local region of stationarity (LRS) [30], and spectral divergence (SD) [31]. Here, we use the LRS method and consider stationary time as the longest time interval during which the correlation coefficient of two delay PSDs exceeds a specified threshold. The correlation coefficient of two delay PSDs can be obtained as

$$\begin{aligned}&R_{\Lambda,qp}\left(t,f;\Delta t\right)\\&=\frac{\int S_{qp}\left(t,f;\tau\right)S_{qp}\left(t+\Delta t,f;\tau\right)d\tau}{\max\left\{\int S_{qp}(t,f;\tau)^2d\tau,\int S_{qp}(t+\Delta t,f;\tau)^2d\tau\right\}}.\end{aligned}\tag{35}$$

Therefore, the stationary time can be calculated as

$$I_{t,qp}\left(t,f\right)=\max\left\{\Delta t|R_{\Lambda,qp}\left(t,f;\Delta t\right)\geq c_{\text{thresh\_IT}}\right\}.\tag{36}$$

Here, $c_{\text{thresh\_IT}}$ is usually set as 0.8 [32].

The definition of stationary time in time domain can be extended to the space and frequency domains. For example, [34] proposed the correlation coefficient of two channels in STF domains, which is defined as the normalized ACF of the delay PSDs of two channels, given by

$$\begin{aligned}&R_{\Lambda qp,\tilde{q}\tilde{p}}\left(t,f;\Delta r^T,\Delta r^R,\Delta t,\Delta f\right)=\\&\frac{\int S_{qp}\left(t,f;\tau\right)S_{\tilde{q}\tilde{p}}\left(t+\Delta t,f+\Delta f;\tau\right)d\tau}{\max\left\{\int S_{qp}(t,f;\tau)^2d\tau,\int S_{\tilde{q}\tilde{p}}(t+\Delta t,f+\Delta f;\tau)^2d\tau\right\}}.\end{aligned}\tag{37}$$

In the time domain, substituting $\tilde{p}=p,\tilde{q}=q$, namely $\Delta r^T=0$, $\Delta r^R=0$, and $\Delta f=0$ into (37), and then the stationary time can be obtained. It is consistent with (36).

In the space domain, substituting $\Delta t=0$, $\Delta f=0$, and $\Delta r^R=0$ into (37), we can get the Tx-side correlation coefficient as

$$\begin{aligned}&R_{\Lambda qp,\tilde{p}}\left(t,f;\Delta r^T\right)\\&=\frac{\int S_{qp}\left(t,f;\tau\right)S_{q\tilde{p}}\left(t,f;\tau\right)d\tau}{\max\left\{\int S_{qp}(t,f;\tau)^2d\tau,\int S_{q\tilde{p}}(t,f;\tau)^2d\tau\right\}}.\end{aligned}\tag{38}$$

Then the Tx-side stationary distance can be written as

$$I_{s,qp,\tilde{p}}^{T}\left(t,f\right)=\max\left\{\Delta r^T\middle|R_{\Lambda qp,\tilde{p}}\left(t,f;\Delta r^T\right)\geq c_{\text{thresh\_IST}}\right\}.\tag{39}$$

Similarly, we can get the Rx-side stationary distance $I_{s,qp,\tilde{q}}^{R}\left(t,f\right)$. Also, substituting $\Delta t=0$, $\Delta r^T=0$, and $\Delta r^R=0$ into (37), the correlation coefficient in the frequency domain can be calculated as

$$\begin{aligned}&R_{\Lambda,qp}\left(t,f;\Delta f\right)\\&=\frac{\int S_{qp}\left(t,f;\tau\right)S_{qp}\left(t,f+\Delta f;\tau\right)d\tau}{\max\left\{\int S_{qp}(t,f;\tau)^2d\tau,\int S_{qp}(t,f+\Delta f;\tau)^2d\tau\right\}}.\end{aligned}\tag{40}$$

Then, we can obtain the stationary bandwidth as

$$I_{f,qp}\left(t,f\right)=\max\left\{\Delta f|R_{\Lambda,qp}\left(t,f;\Delta f\right)\geq c_{\text{thresh\_IF}}\right\}.\tag{41}$$

F. LCRs and AFDs in STF Domains

Based on the CTF in (8), the amplitude PDFs and phase PDFs of the received complex envelope in space, time, and frequency domains can be obtained. In this subsection, for a better understanding, we assume that the t and f in (8) are constants when we discuss the space-domain amplitude PDF, phase PDF, LCR, and AFD. We assume p, q, and f in (8) are constants when we analyze these statistical properties in the time domain. Also, we assume p, q, and t in (8) are constants when we deal with frequency-domain statistical properties. Therefore, the signal amplitude and phase are $\xi(t)$ and $\theta(t)$, and the amplitude PDF and phase PDF will accordingly be $p_\xi(\xi_t, t)$ and $p_\theta(\theta_t, t)$ in the time domain. Then, we can get the time-domain LCR and AFD according to the amplitude PDF and joint PDF of the amplitude and the amplitude slope.

The temporal LCR [33] describes the time-variance of a fading channel by determining the rate of change of the signal amplitude in time. It is defined as the average number of crossings per second at which a fading signal amplitude passing through a certain signal level L_t in the positive (or negative) direction. Mathematically, it is given as

$$\mathcal{N}_\xi(L_t, t) = \int_0^\infty \dot{\xi} p_{\xi\dot{\xi}}(L_t, \dot{\xi}) d\dot{\xi} \tag{42}$$

where $\dot{\xi} = d\xi/dt$ is the derivative of time (amplitude slope) and $p_{\xi\dot{\xi}}(L_t, \dot{\xi})$ is the joint PDF $p_{\xi\dot{\xi}}(\xi, \dot{\xi})$ of ξ and $\dot{\xi}$ that the signal crosses the level L_t. Using results in [35], $\mathcal{N}_\xi(L_t, t)$ can be derived as

$$\begin{aligned}\mathcal{N}_\xi(L_t, t) = & \frac{2L_t\sqrt{K(t)+1}}{\pi^{3/2}} \sqrt{\frac{b_2(t)}{b_0} - \frac{b_1^2(t)}{b_0^2}} e^{-K(t)-(K(t)+1)L_t^2} \\ & \cdot \int_0^{\pi/2} \cosh(2\sqrt{K(t)(K(t)+1)} L_t \cos\theta) \\ & \cdot [e^{-(\chi(t)\sin\theta)^2} + \sqrt{\pi}\chi(t)\sin\theta \operatorname{erf}(\chi(t)\sin\theta)] d\theta \end{aligned} \tag{43}$$

where $\cosh(\cdot)$ is the hyperbolic cosine function and $\operatorname{erf}(\cdot)$ is the error function. Here, $\chi(t)$ and $b_l(t)$ $(l = 0, 1, 2)$ are obtained as

$$\chi(t) = \sqrt{\frac{K(t) \cdot b_1^2(t)}{b_0 \cdot b_2(t) - b_1^2(t)}} \tag{44}$$

and

$$b_l(t) = \frac{d^l R^N(t; \Delta t)}{j^l d\Delta t^l}, \ l = 0, 1, 2. \tag{45}$$

Here, we assume that the p, q, and f are constants in the calculation. Hence the TACF for the NLoS components is $R^N(t; \Delta t)$.

Although the LCR is usually calculated in the time domain, it can be extended to the frequency and space domains [36], [37]. The frequency LCR $\mathcal{N}_\xi(L_f, f)$, Tx-side spatial LCR $\mathcal{N}_{\xi,q}(L_s, r^T)$, and Rx-side spatial LCR $\mathcal{N}_{\xi,p}(L_s, r^R)$ refer to the average times the signal crosses a given threshold in the positive or negative direction per frequency or distance unit. Here, r^T (r^R) is the space-domain variable observed at the Tx (Rx) side. $\mathcal{N}_\xi(L_f, f)$, $\mathcal{N}_{\xi,q}(L_s, r^T)$, and $\mathcal{N}_{\xi,p}(L_s, r^R)$ can be obtained by replacing $R^N(t; \Delta t)$ with $R^N(f; \Delta f)$, $R^N_{qp,\tilde{p}}(\Delta r^T)$, and $R^N_{qp,\tilde{q}}(\Delta r^R)$ in (45).

The temporal AFD is defined as the average time the signal amplitude is below a certain threshold value L_t. Mathematically, it is

$$\mathcal{T}_\xi(L_t, t) = \frac{\int_0^{L_t} p_\xi(\xi_t, t) d\xi}{\mathcal{N}_\xi(L_t, t)} \tag{46}$$

where $p_\xi(\xi_t, t)$ is the PDF of the signal amplitude.

Also, frequency AFD (average fading bandwidth) $\mathcal{T}_\xi(L_f, f)$ and spatial AFDs (average fading distances) at the Tx and Rx sides $\mathcal{T}_{\xi,q}(L_s, r^T)$ and $\mathcal{T}_{\xi,p}(L_s, r^R)$ can be defined as the average bandwidth and the average distances at both Tx and Rx sides signal remains below the threshold value. In summary, temporal LCR and AFD (frequency LCR and AFD, spatial LCR and AFD) can characterize the time-variance (frequency-variance, space-variance) of a fading channel.

III. RESULTS AND DISCUSSIONS

In this section, analytical results, simulation results, and the corresponding measurement results for the channel statistical properties will be discussed and compared. The analytical results were obtained through the plot of the theoretical derivation results of the statistical properties in Section III, while the simulation results were obtained by simulating the corresponding statistical properties of the channel model based on the CIR or the Fourier transform of the CIR. Good consistency of the analytical result and the simulation result can illustrate the correctness of both mathematical derivations of the model and simulation. Then, the analytical/simulation results fit measurement data well, showing the validity of the proposed channel model in terms of the corresponding channel statistical property.

The 6GPCM provides different parameter sets for different frequency bands and scenarios. Those parameters can be adjusted based on measurement data when there is channel measurement. Firstly, user defined parameters, such as carrier frequency, antenna related parameters, positions of the Tx/Rx, and velocities of the Tx/Rx/clusters are set on the basis of real measurements. In the simulation, the uniform linear arrays (ULAs) are employed at both the Tx and Rx sides. Then, parameters that have no/neglected effect on the observed statistical property according to theoretical derivation results in Section III are set to constants. After most parameters are determined, some parameters such as scatterers distribution related parameters are optimized using the minimum mean square error (MMSE) criterion when suitable channel measurement data are used. Otherwise, parameters are chosen to be the same as those of 6GPCM in [14].

Fig. 4 (a) and Fig. 4 (b) show the SCCFs of the channels at different carrier frequencies with fixed and half-wavelength antenna spacing at the Tx side, respectively. Among them, we set the antenna spacing as half wavelength of the minimum carrier frequency for the fixed antenna spacing, and half wavelength of carrier frequencies for the relative antenna spacing. Also, analytical results, simulation results, and the measurement results are compared. Firstly, good consistencies between analytical/simulation results with measurement results in Fig. 4 (a) and Fig. 4 (b) verify the correctness of the 6GPCM. Here, the measurement was conducted in a static court yard

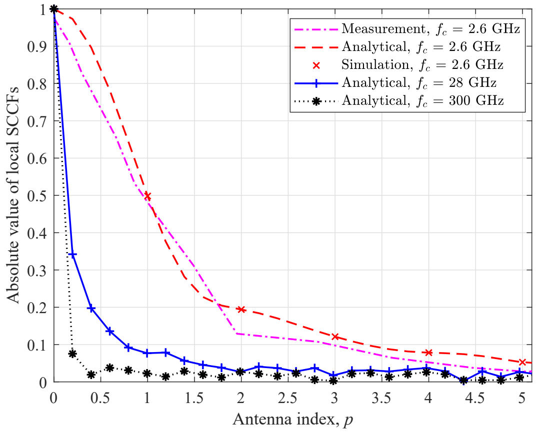

(a) Fixed antenna spacing

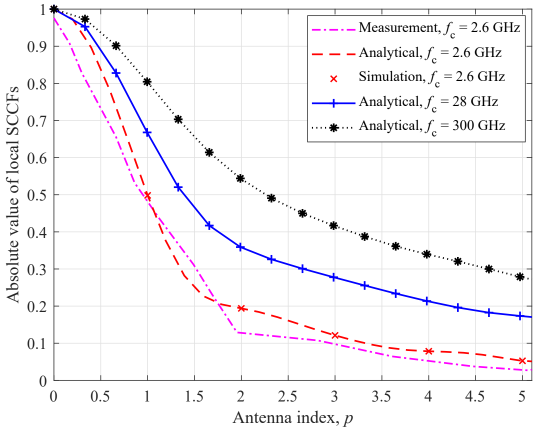

(b) Half-wavelength antenna spacing

Fig. 4. SCCFs at different carrier frequencies with fixed antenna spacing and half-wavelength antenna spacing at the Tx side ($M_T = 128, M_R = 1, v^T = v^R = 0$ m/s, $\beta_A^T = \pi/6, \beta_A^R = \beta_E^T = \beta_E^R = \pi/10, Z_n \sim N(0,3)$, mean$(d_{m_n}^T) = 60$ m, min$(d_{m_n}^T) = 10$ m, $\sigma_x^T = \sigma_x^R = 7$ m, $\sigma_y^T = \sigma_y^R = 12$ m, $\sigma_z^T = \sigma_z^R = 9$ m).

scenario at 2.6 GHz with 128-elements Tx antenna array [38], i.e., $f_c = 2.6$ GHz, $M_T = 128$, and $v^T = v^R = 0$ m/s. Also, we set Rx-side channel model parameters which have no/negligible effect on Tx-side SCCF to constants, i.e., $M_R = 1$, $\beta_A^R = \beta_E^R = \pi/10$, $\sigma_x^R = 7$ m, $\sigma_y^R = 12$ m, $\sigma_z^R = 9$ m and so on. Then we adjust parameters related to cluster distribution at the Tx side, i.e., mean$(d_{m_n}^T)$, min$(d_{m_n}^T)$, σ_x^T, σ_y^T, and σ_z^T. Finally, after optimal parameters searching using the MMSE criterion, we set mean$(d_{m_n}^T) = 60$ m, min$(d_{m_n}^T) = 10$ m, $\sigma_x^T = 7$ m, $\sigma_y^T = 12$ m, $\sigma_z^T = 9$ m, which are reasonable in the court yard scenario. After fitting with measurement data, we simulated the effects of different carrier frequencies (2.6 GHz at sub-6 GHz band, 26 GHz at the mmWave band, and 300 GHz at the THz band) on SCCF. As shown in Fig. 4 (a), the SCCF of the channel decreases with the increase of carrier frequency. In addition, the SCCF of the channel increases with the increase of carrier frequency in Fig. 4 (b), as the increased frequency reduces the spacing between antennas, resulting in the increase of the SCCF. Note that, when analyzing the influence of carrier frequency on the SCCF in Table II later, we use the half-wavelength antenna spacing.

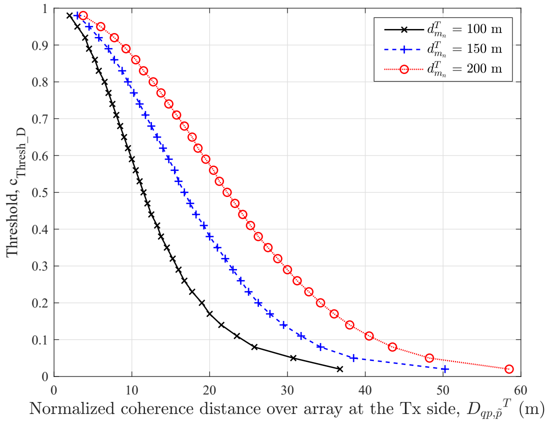

Fig. 5. Coherence distances with different distances from Tx to scatterers ($M_T = 128, M_R = 1, v^T = v^R = 0$ m/s$, \beta_A^T = \pi/2, \beta_A^R = \pi/4, \beta_E^T = \beta_E^R = \pi/10, Z_n \sim N(0,3), \sigma_x^T = \sigma_x^R = 30$ m$, \sigma_y^T = \sigma_y^R = 50$ m$, \sigma_z^T = \sigma_z^R = 40$ m).

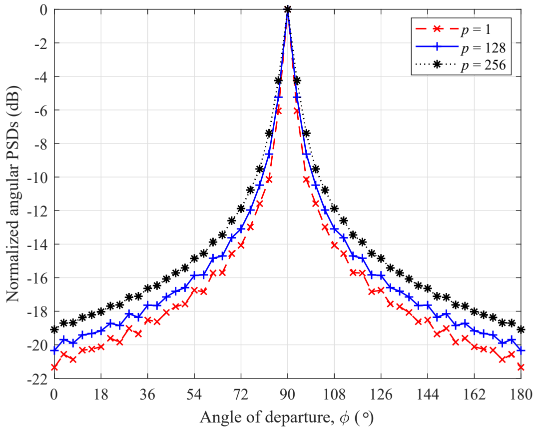

Fig. 6. Angular PSDs of different antenna elements at the Tx side ($M_T = 256, M_R = 1, v^T = v^R = 0$ m/s$, \beta_A^T = \beta_A^R = \pi/4, \beta_E^T = \beta_E^R = \pi/10, Z_n \sim N(0,3), \sigma_x^T = \sigma_x^R = 3$ m$, \sigma_y^T = \sigma_y^R = 5$ m$, \sigma_z^T = \sigma_z^R = 4$ m).

Coherence distances with different distances from Tx to scatterers are as shown in Fig. 5. Here, we use analytical results, which can be calculated according to (18). Since we can obtain the coherence distance based on SCCF, we utilize the similar parameter values as SCCFs in Fig. 4 except for otherwise specified. Note that the coherence distances are normalized w.r.t. antenna spacing. The larger the distance between the scatterers in a cluster and the antenna array, the larger the coherence distance will be, which is consistent with (16). In ultra-massive MIMO scenarios, due to the spherical wavefront property, the angular PSDs of different antenna elements are different, as illustrated in Fig. 6, reflecting non-stationarity in the space domain.

The TACF characterizes the time-varying property of a channel, which is determined by the moving speeds of Tx, Rx, and scatterers in the channel according to (22) and (25). Note that the velocity includes both magnitude and direction of the velocity. The TACFs with different speeds of Rx in the channel is shown in Fig. 7 (a). The measurement [17] was conducted by our group at outdoor UMa scenario in NLoS condition. According to the channel measurement configuration, we set

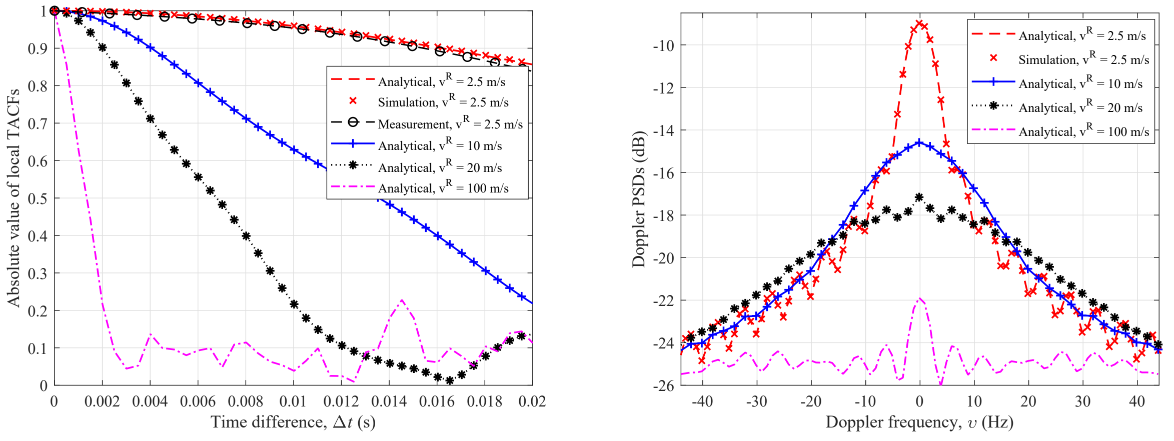

(a) TACFs

(b) Doppler PSDs

Fig. 7. TACFs and Doppler PSDs with different moving speeds of the Rx ($f_c = 5.3$ GHz, $M_T = M_R = 1, v^T = 0$ m/s, $\beta_A^T = \beta_A^R = \pi/4, \beta_E^T = \beta_E^R = \pi/10, \alpha_A^R = \pi/8, \alpha_E^R = 0, \lambda_G = 20$ /m, $\lambda_R = 1$ /m, $D_c^S = 40$ m, $Z_n \sim N(0,3), \sigma_x^T = \sigma_x^R = 3$ m, $\sigma_y^T = \sigma_y^R = 5$ m, $\sigma_z^T = \sigma_z^R = 4$ m).

$f_c = 5.3$ GHz, $\beta_A^T = \beta_A^R = \pi/4$, $\beta_E^T = \beta_E^R = \pi/10$, $v^T = 0$ m/s, $v^R = 2.5$ m/s, $\alpha_A^R = \pi/8$, and $\alpha_E^R = 0$. Here, TACF is a time-domain channel statistical property, so we use the same antenna element pair at the Tx and Rx sides, i.e., $M_T = M_R = 1$. Some parameters were chosen by fitting channel measurement data such as λ_G, λ_R, σ_x^T, σ_x^R, σ_y^T, σ_y^R, σ_z^T, and σ_z^R. The rest parameters were the same as Table IV in [14]. In terms of different speeds, we use 2.5 m/s to simulate pedestrian speed, 10 m/s to simulate driving speed in urban area, 20 m/s to simulate driving speed on highway, and 100 m/s to simulate high-speed train speed. The result shows that the theoretical result, simulation result, and measurement result match very well when the speed of Rx is 2.5 m/s, illustrating the correctness of the model. Also, with the increase of speed, TACF decreases, which is consistent with the theoretical derivation. Moreover, the birth-death process of clusters and the power components in (22) show that TACF is also affected by environmental factors. What's more, we can get the coherence time according to (26) directly. The smaller the TACF, the smaller the corresponding coherence time will be, under the same conditions.

The Doppler PSD characterizes the average power distribution at the Doppler frequency and the Doppler frequency shift of the carrier frequency is caused by the movements of Tx, Rx, and scatterers, as indicated by (28). We also use the same parameters as TACFs in Fig. 7 (a) since we can get Doppler PSD by the Fourier transform of TACF. Fig. 7 (b) shows the Doppler PSDs with different moving speeds of the Rx. We can conclude that the larger the Doppler frequency shift is, the larger the Doppler frequency range of the average power distribution and the smoother the change of Doppler PSD will be. Doppler spread describes the dispersion degree of the Doppler PSD. The greater the Doppler frequency shift caused by motion, the greater the Doppler spread will be. Due to the page limitation, we will not show the simulation results of the coherence time and the RMS Doppler spread here, but from (26) and (29), we know that when TACF decreases, the coherence time will decrease, and the corresponding RMS Doppler spread will increase, as shown in Table II.

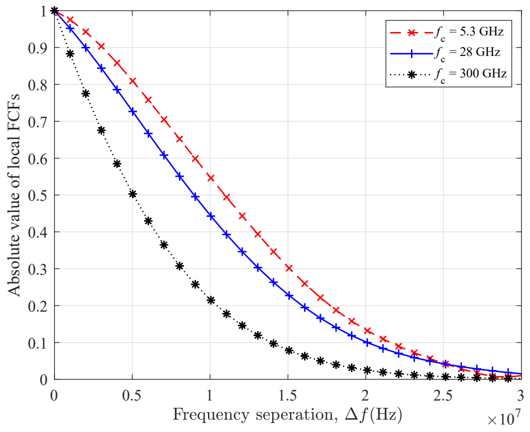

Fig. 8. FCFs at different carrier frequencies ($M_T = M_R = 1, v^T = v^R = 0$ m/s, $\beta_A^T = \beta_A^R = \pi/4, \beta_E^T = \beta_E^R = \pi/10, \alpha_A^R = \pi/8, \alpha_E^R = 0, D_c^S = 40$ m, $Z_n \sim N(0,3), \sigma_x^T = \sigma_x^R = 3$ m, $\sigma_y^T = \sigma_y^R = 5$ m, $\sigma_z^T = \sigma_z^R = 4$ m).

Fig. 8 shows the FCFs and the values of them are different at different carrier frequencies. The FCF measures the frequency correlation of the channel. It can be seen from (30) that FCF of a channel is mainly affected by the value of $\vec{d}_{qp,m_n}(t)$, namely the instantaneous total distance between the Tx, scatterers, and the Rx. Therefore, the distance between the Tx and the Rx, the range of cluster distribution, and the distribution of scatterers within clusters can significantly affect the value of FCF. Furthermore, in the large bandwidth scenarios, channels are non-stationary in the frequency domain [34], that is, the value of FCF is related not only to the frequency interval, but also to the carrier frequency value.

Fig. 9 (a) and Fig. 9 (b) are RMS delay spreads with different clutter densities and different scatterer densities within a cluster in the IIoT scenario. The channel measurements [39] were carried out at 5.85 GHz at light clutter and dense clutter two sub scenarios in the NLoS condition. In the simulation, we set the initial number of clusters $N_c(t_0)$ to 15 and 20 in sparse and dense clutter environments [19], respectively. Also, most parameters were randomly generated according to the 3GPP TR 38.901 channel model [25] for industrial factory scenario.

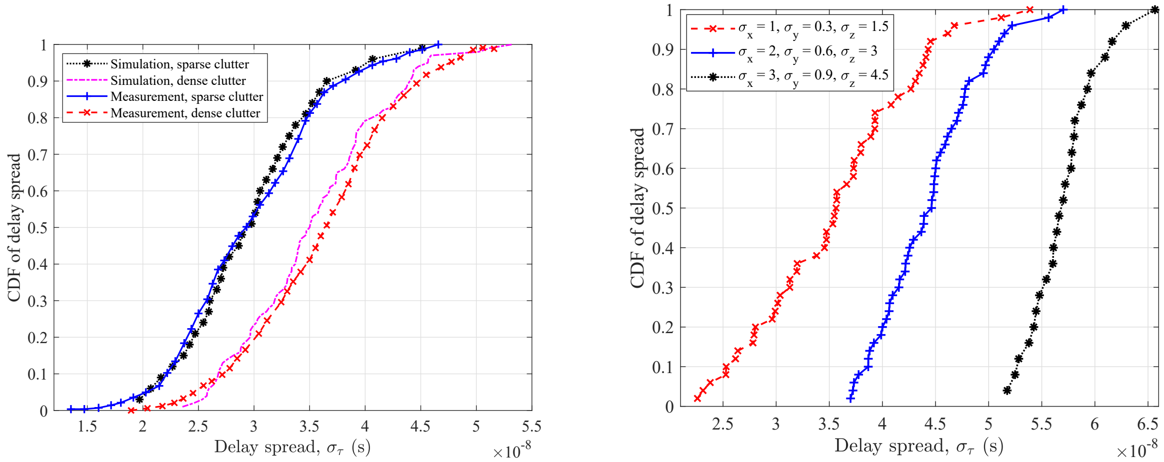

(a) Different clutter densities

(b) Different scatterer densities within a cluster

Fig. 9. RMS delay spreads with different clutter densities and with different scatterer densities within a cluster in the IIoT scenario ($f_c = 5.85$ GHz, $M_R = M_T = 1$, $v^R = 0.4$ m/s, $v^T = v^{A_n} = v^{Z_n} = 0$ m/s, $Z_n \sim N(0,3), \sigma_x^T = \sigma_x^R = 1$ m$, \sigma_y^T = \sigma_y^R = 0.3$ m$, \sigma_z^T = \sigma_z^R = 1.5$ m, $N_c(t_0) = 15$ in (a) and $N_c(t_0) = 20$ in (b)).

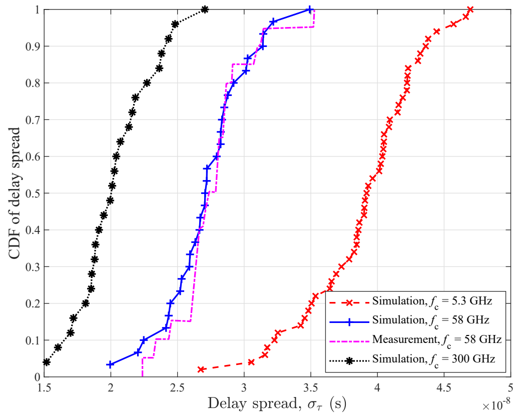

Fig. 10. RMS delay spreads at different frequency bands ($M_T = M_R = 1, v^T = 0$ m/s$, \beta_A^T = \pi/3, \beta_A^R = \beta_E^T = \beta_E^R = \pi/10, v^R = 0.4$ m/s$, \alpha_A^R = \pi/8, \alpha_E^R = 0, Z_n \sim N(0,3), \sigma_x^T = \sigma_x^R = 0.3$ m$, \sigma_y^T = \sigma_y^R = 1$ m$, \sigma_z^T = \sigma_z^R = 1.5$ m).

Then, we fine-tuned the parameters about distributions of scatterers based on channel measurement result, such as σ_x^T, σ_y^T, and σ_z^T at the Tx side and σ_x^R, σ_y^R, and σ_z^R at the Rx side. Since the parameters can significantly affect the RMS delay spread according to theoretical derivation results in Section III. Fig. 9 (a) shows that the channel in dense clutter environment has a larger RMS delay spread. Fig. 9 (b) shows the influence of the dispersion degree of the scatterers in the cluster under the same number of scatterers. The more discrete the scatterer distribution or the more dispersed the value of delay is, the greater the RMS delay spread will be. In (34), we know that RMS delay spread measures the dispersion degree of power in time delay, i.e., $\tau_{qp,m_n}(t)$, whereas the distribution of $\tau_{qp,m_n}(t)$ is directly affected by multipath. Thus, the sparse clutter and dense clutter environments in IIoT scenarios at the same frequency are used as examples to illustrate the impact of obstacle density in the environment on RMS delay spread.

In addition, Fig. 10 shows different RMS delay spreads at different frequency bands, i.e., 5.3 GH, 58 GHz, and 300 GHz. Here, the measurement data were obtained in a laboratory room using 58 GHz carrier frequency [40]. We can see that the measurement result and simulation result fit well, which shows the accuracy of the model. Also, the simulation results show that, with the increase of frequency band, the value of RMS delay spread decreases.

Fig. 11 compares the analytical results with the measurement result for the LCRs in STF domains. The measurement data shown in Fig. 11 (b) was obtained in [41], which was conducted in the HST scenario at 930.2 MHz and the speed of the HST is about 300 km/h. The match between the analytical result and the measurement result verifies the correctness of the 6GPCM. Also, Fig. 11 (a) is the LCR in the space domain. We can see that, the elevation angle of the antenna array at the Tx side affects the Tx-side spatial LCR. Here, we increase this elevation angle to make the angle between the antenna array and the departure wave larger, which will increase the LCR. Moreover, Fig. 11 (b) shows the LCR in the time domain at a HST scenario. As the speed decreases, the LCR decreases. The results are consistent with the theoretical derivation results in (42). In addition, LCR in the frequency domain in Fig. 11 (c) shows that as the dispersion of clusters increase, the frequency LCR increases.

In summary, relationships between statistical properties and the channel parameters are given in Table II. In the table, DS means the delay spread, ASD means the azimuth spread of departure, ESD means the elevation spread of departure, "↑" means increase, "↓" means decrease, and "–" means no impact or negligible impact. Note that Table II only considers the Tx side. The Rx side is similar and is not discussed here.

In addition, channel parameters are seriously affected by the environment, i.e., parameters extracted from channel measurement. For example, authors in [42] conducted measurements in five different factory halls and found that the material of the wall and the density and the positions of objects in the factory halls have a great influence on the number of multipath components in the channel at IIoT scenarios. In [43], the authors carried out the channel measurements in wooded, rural,

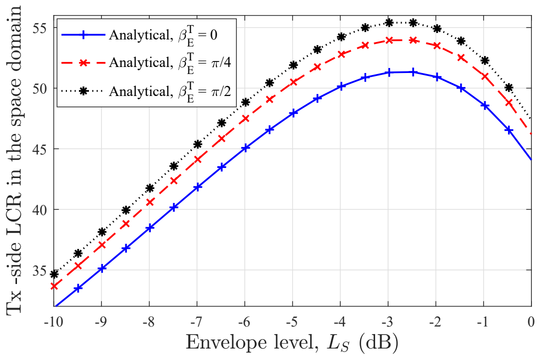

(a) LCR in the space domain

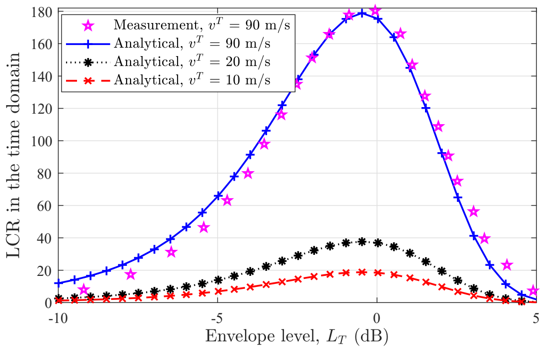

(b) LCR in the time domain

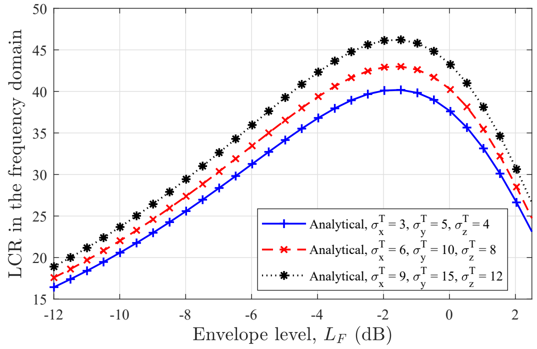

(c) LCR in the frequency domain

Fig. 11. LCRs in space, time, and frequency domains ($f_c = 2.5$ GHz, $M_T = 1, M_R = 1, v^T = v^R = 0$ m/s, $\beta_A^T = \pi/4, \beta_A^R = \beta_E^T = \beta_E^R = \pi/10, Z_n \sim N(0,3), \sigma_x^T = \sigma_x^R = 3$ m, $\sigma_y^T = \sigma_y^R = 5$ m, $\sigma_z^T = \sigma_z^R = 4$ m. Especially, $f_c = 930.2$ MHz, $K = 5.514, v^{Zn} \sim U(0,5)$ m/s in (b)).

suburban, and urban, four different environments mimicking satellite scenarios and draw the conclusion that the RMS delay spread values for suburb and urban environments are larger than those for wooded and rural environments. Also, channel parameters are affected by different frequency bands. For instance, channels at the THz band normally have a larger number of multipath components than channels at sub-6 GHz and mmWave frequency bands, since the wavelength of the THz wave is at the same order as the roughness of objects in the environment, so that there is a larger proportion of diffuse rays at THz frequency band [34]. Further, channel parameters will affect channel statistical properties and communication system performance as mentioned above.

IV. CONCLUSIONS

In this paper, we have conducted a complete study of STF statistical properties of the 6GPCM, which characterized wireless channels for all spectra from the sub-6 GHz to VLC bands and all scenarios such as (ultra-)massive MIMO, HST, IIoT, and UAV scenarios in 6G wireless communication systems. Also, mathematical expressions have been derived for those statistical properties, i.e., STFCF, SCCF, TACF, FCF, angular/Doppler/delay PSDs, RMS angular/Doppler/delay spreads, coherence distance/time/bandwidth, stationary distance/time/bandwidth, and LCRs/AFDs in STF domains. Then, we have classified them according to their relationships. Also, we have explored and summarized the mapping between channel model parameters and these statistical properties at different frequency bands and scenarios through theoretical derivations and simulations. It has been shown that the space/angle-domain statistical properties and the frequency/delay-domain statistical properties are more affected by the carrier frequency, orientation of the antenna array, and propagation scenario. The moving speeds of Tx, Rx, and scatterers in the channel have a significant impact on channel statistical properties in the time/Doppler frequency domain. The work lays a solid foundation for 6G channel model standardization and system design.

REFERENCES

[1] T. S. Rappaport *et al.*, “Wireless communications and applications above 100 GHz: Opportunities and challenges for 6G and beyond,” *IEEE Access*, vol. 7, pp. 78729–78757, 2019.

[2] H. Burchardt, N. Serafimovski, D. Tsonev, S. Videv, and H. Haas, “VLC: Beyond point-to-point communication,” *IEEE Commun. Mag.*, vol. 52, no. 7, pp. 98–105, July 2014.

[3] H. Sarieddeen, M.-S. Alouini and T. Y. Al-Naffouri, “Terahertz-band ultra-massive spatial modulation MIMO,” *IEEE J. Sel. Areas Commun.*, vol. 37, no. 9, pp. 2040–2052, Sept. 2019.

[4] X. Pei *et al.*, “RIS-aided wireless communications: Prototyping, adaptive beamforming, and indoor/outdoor field trials,” *IEEE Trans. Commun.*, vol. 69, no. 12, pp. 8627–8640, Dec. 2021.

[5] C.-X. Wang *et al.*, “On the road to 6G: Visions, requirements, key technologies and testbeds,” *IEEE Commun. Surveys Tuts.*, vol. 25, no. 2, pp. 905–974, 2nd Quart. 2023.

[6] J. C. Reyes-Guerrero, M. Bruno, L. A. Mariscal, and A. Medouri, “Buoy-to-ship experimental measurements over sea at 5.8 GHz near urban environments,” in *Proc. MMS’11*, Hammamet, Tunisia, Sept. 2011, pp. 320–324.

[7] C.-X. Wang, J. Huang, H. Wang, X.-Q. Gao, X.-H. You, and Y. Hao, “6G wireless channel measurements and models: Trends and challenges,” *IEEE Veh. Technol. Mag.*, vol. 15, no. 4, pp. 22–32, Dec. 2020.

[8] J. Bian, C.-X. Wang, X.-Q. Gao, X.-H. You, and M. Zhang, “A general 3D non-stationary wireless channel model for 5G and beyond,” *IEEE Trans. Wireless Commun.*, vol. 20, no. 5, pp. 3211–3224, May 2021.

[9] Q. Zhu, N. Cheng, X. Chen, W. Zhong, B. Hua, and Y. Wang, “Envelope level crossing rate and average fade duration of a generic 3D non-stationary UAV channel model,” *IEEE Access*, vol. 8, pp. 143134–143143, Aug. 2020.

[10] R. Zhang, X. Lu, J. Zhao, L. Cai, and J. Wang, “Measurement and modeling of angular spreads of three-dimensional urban street radio channels,” *IEEE Trans. Veh. Technol.*, vol. 66, no. 5, pp. 3555–3570, May 2017.

[11] B. H. Fleury, “First- and second-order characterization of direction dispersion and space selectivity in the radio channel,” *IEEE Trans. Inf. Theory*, vol. 46, no. 6, pp. 2027–2044, Sept. 2000.

[12] Y. Liu, C.-X. Wang, C. F. Lopez, G. Goussetis, Y. Yang and G. K. Karagiannidis, “3D non-stationary wideband tunnel channel models for 5G high-speed train wireless communications,” *IEEE Trans. Intell. Transp. Syst.*, vol. 21, no. 1, pp. 259–272, Jan. 2020.

TABLE II
RELATIONSHIPS BETWEEN STATISTICAL PROPERTIES AND THE CHANNEL PARAMETERS AT THE TX SIDE.

Parameters Statistics	f_c ↑	v_T/v_{A_n} ↑	M_T ↑	D ↑	number of multipaths ↑	σ_x, σ_y, and σ_z ↑	DS ↑	ASD ↑	ESD ↑
Tx-side SCCF	↑	–	↓	–	–	↓	↓	↓	↓
Tx-side AoD PSD	↑	–	↓	–	–	↓	↓	↓	↓
RMS AoD spread	↓	–	↑	–	–	↑	↑	↑	↑
Tx-side coherence distance	↑	–	↓	–	–	↓	↓	↓	↓
TACF	↓	↓	–	–	–	–	–	–	–
Doppler PSD	↓	↓	–	–	–	–	–	–	–
RMS Doppler spread	↑	↑	–	–	–	–	–	–	–
Coherence time	↓	↓	–	–	–	–	–	–	–
FCF	↓	–	–	↓	↓	↓	↓	↓	↓
Delay PSD	↓	–	–	↓	↓	↓	↓	↓	↓
RMS delay spread	↓	–	–	↑	↑	↑	↑	↑	↑
Coherence bandwidth	↓	–	–	↓	↓	↓	↓	↓	↓
Stationary distance	↑	–	↓	–	–	↓	↓	↓	↓
Stationary time	↓	↓	–	–	–	–	–	–	–
Stationary bandwidth	↓	–	–	↓	↓	↓	↓	↓	↓
Tx-side spatial LCR	↓	–	↑	–	–	↑	↑	↑	↑
Temporal LCR	↑	↑	–	–	–	–	–	–	–
Frequency LCR	↑	–	–	↑	↑	↑	↑	↑	↑

[13] C. Stefanovic, S. Panic, V. Bhatia, and N. Kumar, "On second-order statistics of the composite channel models for UAV-to-ground communications with UAV selection," *IEEE Open J. Commun. Soc.*, vol. 2, pp. 534–544, Mar. 2021.

[14] C.-X. Wang, Z. Lv, X.-Q. Gao, X.-H. You, Y. Hao, and H. Haas, "Pervasive wireless channel modeling theory and applications to 6G GBSMs for all frequency bands and all scenarios," *IEEE Trans. Veh. Technol.*, vol. 71, no. 9, pp. 9159–9173, Sept. 2022.

[15] X. Zhu, C.-X. Wang, J. Huang, M. Chen, and H. Haas, "A novel 3D non-stationary channel model for 6G indoor visible light communication systems," *IEEE Trans. Wireless Commun.*, vol. 21, no. 10, pp. 8292–8307, Oct. 2022.

[16] Y. He, C.-X. Wang, H. Chang, J. Huang, J. Sun, W. Zhang, and H. Aggoune, "A novel 3D non-stationary maritime wireless channel model," *IEEE Trans. Commun.*, vol. 70, no. 3, pp. 2102–2116, Mar. 2022.

[17] Y. Zheng, C.-X. Wang, R. Yang, L. Yu, F. Lai, J. Huang, R. Feng, C. Wang, C. Li, and Z. Zhong, "Ultra-massive MIMO channel measurements at 5.3 GHz and a general 6G channel model," *IEEE Trans. Veh. Technol.*, vol. 72, no. 1, pp. 20–34, Jan. 2023.

[18] Y. Sun, C.-X. Wang, J. Huang, and J. Wang, "A 3D non-stationary channel model for 6G wireless systems employing intelligent reflecting surfaces with practical phase shifts," *IEEE Trans. Cog. Commun. Netw.*, vol. 7, no. 2, pp. 496–510, June 2021.

[19] Y. Li, C.-X. Wang, and Y. Liu, "A 3D non-stationary geometry-based stochastic model for industrial automation wireless communication systems," in *Proc. IEEE PIMRC'21*, online, Sept. 2021, pp. 1–6.

[20] P. Kyösti *et al.*, "WINNER II channel models," IST-4-027756, WINNER II D1.1.2, v1.2, Apr. 2008.

[21] ITU-R, "Preliminary draft new report ITU-R M. [IMT-2020.EVAL]," Niagara Falls, Canada, R15-WP5D-170613-TD-0332, June 2017.

[22] R. Olsen, D. Rogers, and D. Hodge, "The aR^b relation in the calculation of rain attenuation," *IEEE Trans. Antennas Propag.*, vol. 26, no. 2, pp. 318–329, Mar. 1978.

[23] M. T. Barros, R. Mullins, and S. Balasubramaniam, "Integrated terahertz communication with reflectors for 5G small-cell networks," *IEEE Trans. Veh. Technol.*, vol. 66, no. 7, pp. 5647–5657, July 2017.

[24] 3GPP TR 38.811. "Study on new radio (NR) to support non-terrestrial networks (Release 16)," Sept. 2019.

[25] *Study on Channel Model for Frequencies From 0.5 to 100 GHz (Release 16)*, document TR 38.901, V16.1.0, 3GPP, Nov. 2020.

[26] C. Han, A. O. Bicen, and I. F. Akyildiz, "Multi-ray channel modeling and wideband characterization for wireless communications in the terahertz band," *IEEE Trans. Wireless Commun.*, vol. 14, no. 5, pp. 2402–2412, May 2015.

[27] R. C. Qiu, "A study of the ultra-wideband wireless propagation channel and optimum UWB receiver design," *IEEE J. Sel. Areas Commun.*, vol. 20, no. 9, pp. 1628–1637, Dec. 2002.

[28] J. Cai, W. Song, and Z. Li, "Doppler spread estimation for mobile OFDM systems in Rayleigh fading channels," *IEEE Trans. Consumer Electron.*, vol. 49, no. 4, pp. 973–977, Nov. 2003

[29] M. Herdin, N. Czink, H. Ozcelik, and E. Bonek, "Correlation matrix distance, a meaningful measure for evaluation of non-stationary MIMO channels," in *Proc. IEEE VTC 2005-Spring*, Stockholm, Sweden, May 2005, pp. 136–140.

[30] A. Gehring, M. Steinbauer, I. Gaspard, and M. Grigat, "Empirical channel stationarity in urban environments," in *Proc. EPMCC*, Vienna, Austria, Feb. 2001.

[31] T. T. Georgiou, "Distances and riemannian metrics for spectral density functions," *IEEE Trans. Signal Process.*, vol. 55, no. 8, pp. 3995–4003, Aug. 2007.

[32] C. Chen, Z. Zhong, and B. Ai, "Stationarity intervals of time-variant channel in high speed railway scenario," *China Commun.*, vol. 9, no. 8, pp. 64–70, Aug. 2012.

[33] A. Abdi and M. Kaveh, "Level crossing rate in terms of the characteristic function: A new approach for calculating the fading rate in diversity systems," *IEEE Trans. Commun.*, vol. 50, no. 9, pp. 1397–1400, Sept. 2002.

[34] J. Wang, C.-X. Wang, J. Huang, H. Wang, and X.-Q. Gao, "A general 3D space-time-frequency non-stationary THz channel model for 6G ultra-massive MIMO wireless communication systems," *IEEE J. Sel. Areas Commun.*, vol. 39, no. 6, pp. 1576–1589, June 2021.

[35] J. Bian, J. Sun, C.-X. Wang, R. Feng, J. Huang, Y. Yang, and M. Zhang, "A WINNER+ based 3D non-stationary wideband MIMO channel model," *IEEE Trans. Wireless Commun.*, vol. 17, no. 3, pp. 1755–1767, Mar. 2018.

[36] T. R. R. Marins, A. A. Dos Anjos, V. M. Rodrigo Penarrocha, L. Rubio, J. Reig, R. A. A. De Souza, and M. D. Yacoub, "Fading evaluation in the mm-wave band," *IEEE Trans. Commun.*, vol. 67, no. 12, pp. 8725–8738, Dec. 2019.

[37] A. A. Dos Anjos, T. R. R. Marins, C. R. Nogueira da Silva, V. M. Rodrigo Penarrocha, L. Rubio, J. Reig, R. A. A. De Souza, and M. D. Yacoub, "Higher order statistics in a mmWave propagation environment," *IEEE Access*, vol. 7, pp. 103876–103892, Aug. 2019.

[38] S. Payami and F. Tufvesson, "Channel measurements and analysis for very large array systems at 2.6 GHz," in *Proc. 6th Eur. Conf. Antennas Propag. (EUCAP)*, Prague, Czech, Mar. 2012, pp. 433–437.

[39] B. Holfeld *et al.*, "Radio channel characterization at 5.85 GHz for wireless M2M communication of industrial robots," in *Proc. IEEE WCNC'16*, Doha, Qatar, Apr. 2016, pp. 1–7.

[40] P. F. M. Smulders and A. G. Wagemans, "Frequency-domain measurement of the millimeter wave indoor radio channel," *IEEE Trans. Instrum. Meas.*, vol. 44, no. 6, pp. 1017–1022, Dec. 1995.

[41] L. Gao, Z. Zhong, B. Ai, L. Xiong, and H. Zhang, "Analysis and emulation of the small-scale fading characteristics in the high-speed rail scenarios," in *Proc. ICST*, Harbin, China, Aug. 2011, pp. 1181–1185.

[42] S. Jaeckel *et al.*, "Industrial indoor measurements from 2-6 GHz for the

3GPP-NR and QuaDRiGa channel model," in *Proc. IEEE VTC 2019-Fall*, Honolulu, USA, Sept. 2019, pp. 1–7.

[43] E. Cid, M. G. Sanchez, and A. V. Alejos, "Wideband analysis of the satellite communication channel at Ku- and X-bands," *IEEE Trans. Veh. Technol.*, vol. 65, no. 4, pp. 2787–2790, Apr. 2016.

Cheng-Xiang Wang (Fellow, IEEE) received the B.Sc. and M.Eng. degrees in communication and information systems from Shandong University, China, in 1997 and 2000, respectively, and the Ph.D. degree in wireless communications from Aalborg University, Denmark, in 2004.

He was a Research Assistant with the Hamburg University of Technology, Hamburg, Germany, from 2000 to 2001, a Visiting Researcher with Siemens AG Mobile Phones, Munich, Germany, in 2004, and a Research Fellow with the University of Agder, Grimstad, Norway, from 2001 to 2005. He has been with Heriot-Watt University, Edinburgh, U.K., since 2005, where he was promoted to a Professor in 2011. In 2018, he joined Southeast University, Nanjing, China, as a Professor. He is also a part-time Professor with Purple Mountain Laboratories, Nanjing. He has authored 4 books, 3 book chapters, and more than 500 papers in refereed journals and conference proceedings, including 27 highly cited papers. He has also delivered 24 invited keynote speeches/talks and 16 tutorials in international conferences. His current research interests include wireless channel measurements and modeling, 6G wireless communication networks, and electromagnetic information theory.

Dr. Wang is a Member of the Academia Europaea (The Academy of Europe), a Fellow of the Royal Society of Edinburgh (FRSE), IEEE, IET, and China Institute of Communications (CIC), an IEEE Communications Society Distinguished Lecturer in 2019 and 2020, and a Highly-Cited Researcher recognized by Clarivate Analytics in 2017-2020. He is currently an Executive Editorial Committee Member of the IEEE TRANSACTIONS ON WIRELESS COMMUNICATIONS. He has served as an Editor for over ten international journals, including the IEEE TRANSACTIONS ON WIRELESS COMMUNICATIONS, from 2007 to 2009, the IEEE TRANSACTIONS ON VEHICULAR TECHNOLOGY, from 2011 to 2017, and the IEEE TRANSACTIONS ON COMMUNICATIONS, from 2015 to 2017. He was a Guest Editor of the IEEE JOURNAL ON SELECTED AREAS IN COMMUNICATIONS, Special Issue on Vehicular Communications and Networks (Lead Guest Editor), Special Issue on Spectrum and Energy Efficient Design of Wireless Communication Networks, and Special Issue on Airborne Communication Networks. He was also a Guest Editor for the IEEE TRANSACTIONS ON BIG DATA, Special Issue on Wireless Big Data, and is a Guest Editor for the IEEE TRANSACTIONS ON COGNITIVE COMMUNICATIONS AND NETWORKING, Special Issue on Intelligent Resource Management for 5G and Beyond. He has served as a TPC Member, a TPC Chair, and a General Chair for more than 30 international conferences. He received 15 Best Paper Awards from IEEE GLOBECOM 2010, IEEE ICCT 2011, ITST 2012, IEEE VTC 2013 Spring, IWCMC 2015, IWCMC 2016, IEEE/CIC ICCC 2016, WPMC 2016, WOCC 2019, IWCMC 2020, WCSP 2020, CSPS 2021, WCSP 2021, and IEEE/CIC ICCC 2022.

Zhen Lv (Member, IEEE) received the B.Sc. and M.Sc. degrees in Information and Communication Engineering from Shandong University, China, in 2015 and 2018, respectively. She is currently a wireless channel engineer with the Purple Mountain Laboratories, Nanjing, China. Her research interests include 6G wireless channel modeling and channel simulator.

Yunfei Chen (Senior Member, IEEE) received his B.E. and M.E. degrees in electronics engineering from Shanghai Jiaotong University, Shanghai, P.R.China, in 1998 and 2001, respectively. He received his Ph.D. degree from the University of Alberta in 2006. He is currently working as a Professor in the Department of Engineering at the University of Durham, U.K. His research interests include wireless communications, performance analysis, joint radar communications designs, cognitive radios, wireless relaying and energy harvesting.

Harald Haas (Fellow, IEEE) received the Ph.D. degree from The University of Edinburgh in 2001. He is a Distinguished Professor of Mobile Communications at The University of Strathclyde/Glasgow, Visiting Professor at the University of Edinburgh and the Director of the LiFi Research and Development Centre. Prof. Haas set up and co-founded pureLiFi. He currently is the Chief Scientific Officer. He has co-authored more than 600 conference and journal papers. He has been among the Clarivate/Web of Science highly cited researchers between 2017-2021. Haas' main research interests are in optical wireless communications and spatial modulation which he first introduced in 2006. In 2016, he received the Outstanding Achievement Award from the International Solid State Lighting Alliance. He was the recipient of IEEE Vehicular Society James Evans Avant Garde Award in 2019. In 2017, he received a Royal Society Wolfson Research Merit Award. He was the recipient of the Enginuity The Connect Places Innovation Award in 2021. He is a Fellow of the IEEE, the Royal Academy of Engineering (RAEng), the Royal Society of Edinburgh (RSE) as well as the Institution of Engineering and Technology (IET).